Oscillatory climate modes in the Eastern Mediterranean: Synchronization with the NAO and Southern Oscillation

Yizhak Feliks[1] Michael Ghil[2,3] and Andrew W. Robertson[4]

Dept. of Atmospheric & Oceanic Sciences and Institute of Geophysics & Planetary Physics, University of California, Los Angeles, USA

[1]Permanent address: Department of Mathematics, Israel Institute of Biological Research, Ness Ziona, Israel
[2]Additional affiliation: Geosciences Department and Laboratoire de Météorologie Dynamique (CNRS and IPSL), Ecole Normale Supérieure, Paris, France.
[3]Corresponding author, E-mail: ghil@atmos.ucla.edu .
[4]Permanent address: International Research Institute for climate and society (IRI), Monell Building, Room 230, P. O. Box 1000, Palisades, NY 10964-8000, USA

Abstract

Oscillatory climatic modes over the North Atlantic, Ethiopian Plateau, Eastern Mediterranean and the Tropical Pacific Ocean were examined in instrumental and proxy records from these regions. The teleconnections between the regions were studied in terms of synchronization of chaotic oscillators. We modify standard methods for studying synchronization among such oscillators by combining them with advanced spectral methods, including singular spectral analysis. This modification helps test, besides the degree of synchronization, also the strength of the coupling.

A prominent oscillatory mode with a 7-year period was found in all the climatic regions studied here and is completely synchronized with this mode over the North Atlantic. An energy analysis of the synchronization raises the possibility that this mode originates in fact in the North Atlantic. Evidence is discussed for this mode being induced by the 7–8-year oscillation in the position of the Gulf Stream front. A mechanism for the teleconnections between the North Atlantic, Ethiopian Plateau and Eastern Mediterranean is proposed.

An oscillatory mode with a 4-year period was also found in all the regions but cannot be attributed exclusively to the quasi-quadrennial oscillation associated with the El Niño-Southern Oscillation (ENSO). A North–Atlantic-based oscillation with a similar period seems to affect the 4-year mode in the Eastern Mediterranean as well. Over the Ethiopian Plateau we found two oscillatory modes with similar periods: the 3.7-year mode appears to be associated with ENSO, while the 4.2-year mode arises from the mode with this period in the Gulf Stream front.

1. Introduction

Interannual and interdecadal oscillations have been found in many variables and parts of the Earth's climate system; see Dettinger et al. (1995), Plaut et al. (1995), Unal and Ghil (1995), Moron et al. (1998), and many others. These oscillations are usually correlated across large regions, on the order of thousands of kilometers, through "teleconnections" (Wallace and Gutzler, 1981; Barnston and Livezey, 1987) that have been attributed to the propagation of atmospheric Kelvin and Rossby waves, to changes in thermally direct circulations, to intrinsic modes of atmospheric variability, and to effects of changes in the oceans' wind-driven or thermohaline circulation. The terms "teleconnection" and "oscillation" have often been used synonymously in meteorology, ever since the discovery of the North Atlantic, North Pacific and Southern Oscillations by G. Walker and associates (e.g., Walker and Bliss, 1932, 1937), where the term "oscillation" was applied to describe large-scale seesaw patterns in sea level pressure.

The presence of distinct spectral peaks was not implied in these pioneering studies, although Walker (1931) did hint at their presence in the Southern Oscillation (SO). We now know that the SO is strongly coupled to El Niño (EN) sea surface temperature anomalies to form ENSO, which exhibits pronounced interannual periods (Philander, 1990; Jiang et al., 1995a) and has near-global impact through atmospheric teleconnections (Hoskins and Karoly, 1981; Ropelewski and Halpert, 1987; Chiang and Sobel, 2002 Lintner and Chiang, 2007). In the mid-latitudes, the best-known oscillatory patterns are the North Atlantic Oscillation (NAO: Rogers, 1990; Hurrell, 1995) and the Pacific Decadal Oscillation (Mantua et al., 1997; Chao et al., 2000), while the tropics are dominated by ENSO (Rasmusson and Carpenter, 1982; Philander, 1990).

We examine here interannual and interdecadal climate variability over the Eastern Mediterranean during the last two centuries. Several instrumental and proxy records longer than 100 years exist for different sites in the region. The records we analyze include precipitation records from Jerusalem, as well as tree-ring records from the Golan Heights (Feliks, 1968), and the Nile River flow records previously analyzed by Kondrashov et al. (2005). We use advanced spectral methods, including singular-spectrum analysis (SSA), to find the most significant oscillatory modes in these climatic records (Ghil et al., 2002a), and relate them to similar modes in other parts of the world.

We concentrate thus on the Eastern Mediterranean and the Ethiopian Plateau, on the one hand, and on potential teleconnections with the North Atlantic and the Tropical Indo-Pacific Ocean, on the other. Previous teleconnection studies were based on correlations between climatic time series from the regions of interest (Wallace and Gutzler, 1981); often the correlations were no larger than 0.6 and they did not clarify in which frequency band the teleconnection under investigation was most active.

The commonalities between the well-documented records of the NAO index, the Southern Oscillation Index (SOI) and the records representing the focus area of our paper are considered here from the point of view of synchronization between chaotic oscillators (Rosenblum et al., 1996; Duane, 1997; Osipov et al., 2003; Duane and Tribbia, 2004). Our synchronization analysis differs from that of previous studies inasmuch as we use multi-channel SSA (M-SSA) to examine cross-spectra of the climate records from the different regions. Based on this preliminary analysis, significant oscillatory modes are reconstructed and we apply the synchronization analysis to these modes. This approach allows us to identify which regions are teleconnected and, using a novel energy-ratio

criterion, we can determine the strength of the coupling and the region in which each oscillatory mode arises.

In section 2, our modified synchronization analysis is described and it is illustrated by its application to a system of two coupled Rössler oscillators. In section 3, we provide a short analysis of each climate record separately, while in section 4 we examine the synchronization between the records from different regions and consider the mechanism of this synchronization. Concluding remarks appear in section 5.

2. Synchronization of chaotic time series

2.1 General methodology

We follow the overall approach of Rosenblum et al. (1996) and Osipov et al. (2003) in our analysis of the synchronization between two chaotic time series, and will present some new concepts and tools after summarizing their approach. First, these authors, following Gabor (1946) and Panter (1965), define an analytic signal $\psi(t)$ associated with a given time series $x(t)$. This analytic signal is the complex-valued time series

$$\psi(t) = x(t) + iy(t), \tag{1a}$$

where $i = \sqrt{-1}$ is the imaginary unit and

$$y(t) = \pi^{-1} PV \int_{-\infty}^{\infty} \frac{x(s)}{s - t}\, ds \tag{1b}$$

is the Hilbert transform of $x(t)$. The instantaneous amplitude $A(t)$ and phase $\phi(t)$ of the analytic signal $\psi(t)$ are defined by the polar representation of Eq. (1a),

$$\psi(t) = A(t)\exp[i\phi(t)]. \tag{1c}$$

Two signals, $x_1(t)$ and $x_2(t)$ are considered to be synchronized when the phase difference $d(t) = \phi_1(t) - \phi_2(t)$ between the two does not grow with time. Note that the phase angle $\phi(t)$ is allowed to increase beyond 2π.

To get the imaginary part of the analytic signal in Eq. (1b) one takes the Hilbert transform $y(t)$ of the time series $x(t)$ and this involves computing the Cauchy principal value PV of the integral on the right-hand side. The integral is known to be ill posed, and the numerical procedures for regularizing the singularity of this Cauchy principal value are the subject of many papers (e.g., Hasegawa and Torii, 1991; Rosen and Cormack, 1995); a short bibliography can be found at http://math.fullerton.edu/mathews/c2003/cauchyprincipal/CauchyPrincipalValuelBib/Links/CauchyPrincipalValuelBib_lnk_2.html.

The climate records we consider here are short (100–200 years or less) and there are only about 4–10 data points per period of interest. Hence available methods for the reliable calculation of the Hilbert transform do not converge. Moreover, it is well-nigh impossible to test over just a very few full periods whether the phase difference $d(t)$ between two nearly equal periodicities in the time series $x_1(t)$ and $x_2(t)$ does increase with time or not. We use therefore a different approach, in order to find the phase and amplitude of an arbitrary signal; this approach has been tested extensively and found to be useful in studying oscillatory modes present in short and noisy climate records (Ghil et al., 2002a).

The instantaneous phase $\phi_i(t)$ of each signal $\psi_i(t)$ is given, following Plaut and Vautard (1994) and Moron et al. (1998), by

$$\phi_i(t) = \arctan(\psi_i'(t) / \psi_i(t)), \qquad (2)$$

where $\psi'(t)$ is the time derivative of $\psi(t)$, while the instantaneous amplitude $A_i(t)$ is given by the local extremum (maximum or minimum) of the signal that is nearest to the epoch t. The synchronization between two signals is measured by the standard deviation σ of the instantaneous phase difference between the two time series,

$$\sigma^2 = < (d(t) - < d(t) >)^2 >, \qquad (3)$$

and the correlation $cor(A_1, A_2)$ between the instantaneous amplitudes:

$$cor(A_1, A_2) = < A_1 A_2 > / \sqrt{< A_1^2 >< A_2^2 >}. \qquad (4)$$

Following Osipov et al. (2003), one can identify three types of synchronization in chaotic time series, which we label as follows:

(F) synchronization of the frequencies alone, i.e. *frequency locking*; in this case

$$0.5 = \sigma_0 < \sigma < \infty;$$

(FP) synchronization of the phases as well, i.e. *phase locking*,

$$\sigma < \sigma_0 = 0.5;$$

and finally

(FPA) *complete synchronization*, including both phases and amplitudes, so that

$$cor(A_1, A_2) \approx 1.$$

Frequency locking (F) does not imply phase locking (FP), as can be easily seen from adding either a random perturbation or a purely chaotic one — i.e., one with a purely continuous spectrum, like that of the Lorenz (1963) system — to one of two harmonic oscillators having the same frequency. The threshold $\sigma_0 = 0.5$ in (FP) is fairly arbitrary, but clearly much smaller than π. When examining the coupling of two Rössler oscillators,

Rosenblum et al. (1996) found that the strength of the coupling increases from (F) to (FP) and on to (FPA).

The difficulty in estimating the quantities defined in Eqs. (1)–(4) and used in the definitions of synchronization (F)–(FPA) resides in the essential ill-posedness of the differentiation of chaotic time series, especially in the presence of measurement and sampling noise (Maraun and Kurths, 2004). This difficulty has given rise to several different techniques for estimating the phase and amplitude associated with a given time series. To obtain smooth and reliable estimates of these quantities, we apply an advanced, well-documented spectral method to find the oscillatory modes shared by the two time series.

Multi-channel SSA (M-SSA) is an extension of SSA to several time series, with each "channel" corresponding to one of the scalar time series of interest (Broomhead and King, 1986a,b; Keppenne and Ghil, 1993; Plaut and Vautard, 1994; Ghil et al., 2002a). The method essentially diagonalizes the lag-covariance matrix associated with the vector time series whose components are the channels. The eigenvectors of this matrix are the space-time empirical orthogonal functions (ST-EOFs) and projection onto them yields the corresponding principal components.

The entire vector time series or parts thereof that correspond to trends, oscillatory modes or noise can be reconstructed by using linear combinations of these principal components and ST-EOFs, which provide the reconstructed components (RCs). A statistical significance test against red noise is performed by comparing the projection of the data onto a given ST-EOF for each channel with the corresponding projections of a large ensemble of red-noise surrogates (Allen and Robertson, 1996; Ghil et al., 2002a).

In the following application of the M-SSA to our climate records, each channel corresponds to an instrumental or proxy record, and each record is nondimensionalized by its standard deviation. Mostly we will be interested in pairwise or two-channel SSA. Only those signals that are significant at the 95% level will be analyzed further below.

2.2 Application to coupled Rössler oscillators

In this section, we illustrate the modified synchronization analysis method described above by applying it to a system of two coupled Rössler oscillators, and examine the route to synchronization in the parameter range studied by Rosenblum et al. (1996). Janjarasjitt and Loparo (2008) also studied recently a similar coupled system.

The equations of the coupled system are, for $i = 1$ or 2,

$$\begin{aligned} \frac{dx_{1,2}}{dt} &= -\omega_{1,2} y_{1,2} - z_{1,2} + C(x_{2,1} - x_{1,2}) \\ \frac{dy_{1,2}}{dt} &= \omega_{1,2} x_{1,2} + 0.15 y_{1,2} \\ \frac{dz_{1,2}}{dt} &= 0.2 + z_{1,2}(x_{1,2} - 10) \end{aligned} \quad , \qquad (5)$$

where $\omega_1 = 1.015$ and $\omega_2 = 0.985$ are the two angular frequencies of the uncoupled oscillators, and C is the coupling parameter between the two oscillators. We used the Adams-Bashforth scheme to integrate Eqs. (5) with a time step $\delta t = 0.01$, and stored the first components $x_1(t)$ and $x_2(t)$ of the oscillator $i = 1, 2$ every $\Delta t = 0.5$ time units, i.e. every 50 time steps. The synchronization analysis was carried out on the two model-generated time series $x_1(t)$ and $x_2(t)$ in the time interval $t = 1000$–4000.

Applying the synchronization criteria of Eqs. (1)–(4) to the two time series $x_1(t)$ and $x_2(t)$, our results show that, for $C < 0.027$, the two time series are not synchronized at all: the standard deviation σ of the phase differences is large and the amplitude correlation is quite small; see Table 1 and Fig. 1a ($C = 0.017$). For $C = 0.027$, the standard deviation is $\sigma = 7.9$ over the time interval of 3000 time units, which is finite but already quite large (in particular larger than π) and actually tends to infinity as the time interval increases to infinity (not shown), while the amplitude correlation is small, $cor(A_1, A_2) = 0.08$, and does stay so as the interval increases.

When increasing the coupling strength to $C = 0.035$, the standard deviation of the phase difference drops to $\sigma = 0.21$ and changes but little as the time interval increases; thus both the frequencies and phases of the two oscillators are synchronized. On the other hand the amplitude correlation only reaches 0.24, cf. Fig. 1b ($C = 0.035$); so the synchronization type is only (FP), and not (FPA). From Fig. 1b, one sees in fact that the amplitude evolutions of the two series do not match. These results agree with those of Rosenblum et al. (1996).

Next we compute the cross spectra of x_1 and x_2, by applying M-SSA with two channels, using a window width of $M = 60\Delta t = 30$ time units (Ghil et al., 2002a). The RC of an oscillatory mode associated with a given pair $(i, i+1)$ of ST-EOFs will be denoted by $\mathrm{RC}^{(i,\, i+1)}$; the corresponding components will be called $\mathrm{RC}^{(i,\, i+1)}x_1$ for channel x_1 and $\mathrm{RC}^{(i,\, i+1)}x_2$ for channel x_2, and the energy (variance) in each of the two RC components will be identified as $E(\mathrm{RC}^{(i,\, i+1)}x_1)$ and $E(\mathrm{RC}^{(i,\, i+1)}x_2)$, respectively.

For $C = 0.0$, the oscillators are not coupled and we obtain five significant eigenvalues of the lag-covariance matrix: 2 eigenvalues equal to 0.168, 2 equal to 0.162,

and one equal to 0.202; the significance is established with respect to the noise present in the two time series $x_1(t)$ and $x_2(t)$, due to the interaction between the numerical truncation and the nonlinearity (Henrici, 1963; Isaacson and Keller, 1966). The RC associated with the first ST-EOF pair, $RC^{(1,2)}$, captures 51% of the variance and has energy only in $RC^{(1,2)}x_2$. The second significant pair of RCs, $RC^{(3,4)}$, captures 35% of the variance and has energy only in $RC^{(3,4)}x_1$. There is no oscillatory mode that contains energy in both RCx_1 and RCx_2, as expected for the uncoupled system; the two pairs of eigenvalues simply correspond to the values of the frequencies ω_1 and ω_2. The RC associated with the first four modes, $RC^{(1-4)}$, contains 51% + 35% = 86% of the variance. The amplitude correlation between $RC^{(1-4)}x_1$ and $RC^{(1-4)}x_2$ is 0.12, about the same as the amplitude correlation between the complete time series $x_1(t)$ and $x_2(t)$.

By increasing the coupling strength between the two oscillators, the system changes gradually as follows: (a) The five significant eigenvalues become closer in value and merge eventually; for $C = 0.035$, when the system experiences phase synchronization (see again Table 1), these five eigenvalues have completely merged (not shown). (b) The variance of the $RC^{(1,2)}$ oscillatory mode increases and that of the $RC^{(3,4)}$ mode decreases as C increases; see columns 2 and 3 of Table 1. (c) The energy ratio $\varepsilon_{12} = E(RCx_1)/E(RCx_2)$ between the two components of the $RC^{(1,2)}$ oscillatory mode increases and tends to 1.0 as C increases (column 4 of Table 1); the energy ratio $\varepsilon_{34} = E(RCx_1)/E(RCx_2)$ of the $RC^{(3,4)}$ oscillatory mode decreases (from infinity) and also tends to unity as C increases (not shown). The ratio ε_{34} for the oscillatory mode associated with the second pair is almost equal to that associated with the first pair. (d) The standard

deviation of the phase difference σ decreases as C increases (column 5 of Table 1) and we use it to measure the phase synchronization of the system.

The accumulation of the variance in the RC pair (1,2) is clearly of the essence in the synchronization process. The equalization of the energy ratios ε_{12} and ε_{34} between the two components of the $RC^{(1,2)}$ mode and the $RC^{(3,4)}$ mode, respectively, may be due to the symmetry of the coupled system, with two identical Rössler oscillators being involved.

Increasing C from 0.027 to 0.035, the energy in the $RC^{(1,2)}$ mode increases from 86% to 93% and that of the $RC^{(3,4)}$ mode decreases from 9% to 1%, while σ changes from 7.9 to 0.21 (see again Table 1 and Fig. 1), and thus the synchronization type of the system is (FP) for C = 0.035. Increasing C further to 0.12 increases the amplitude correlation from 0.24 to 0.96 (column 6 of Table 1, and Fig. 1c, with C = 0.12) and now the system's synchronization is complete, i.e., of (FPA) type; the two time series are now visually indistinguishable (Fig. 1c).

Thus our conclusions about the synchronization type in the coupled Rössler oscillator pair, as a function of the coupling strength, agree with those of Osipov et al. (1993) and Rosenblum et al. (1996). Their criteria, though, relied on the Lyapunov spectrum, while ours rely on M-SSA, which seems more robust in the analysis of large systems and for short and noisy time series, like those available in climate dynamics and the geosciences in general.

Along the route to synchronization between the coupled Rössler oscillators, and for all values of $C > 0$, the synchronization between the components RCx_1 and RCx_2 that belong to the same oscillatory pair is of complete (FPA) type, since the corresponding σ is quite small, $\sigma << 1$, and the amplitude correlation is about 1. A difference between the

two components persists, though, for low coupling strength and is manifest in the energy ratio $E(\mathrm{RC}x_1)/E(\mathrm{RC}x_2)$: this ratio tends to unity for strong coupling and tends to zero (or infinity) as $C \to 0$. Therefore, in the analysis of the cross-spectra of several pairs of climatic records, we will examine the ratio $\varepsilon = E(\mathrm{RC}x_1)/E(\mathrm{RC}x_2)$ to identify the coupling strength in significant frequency bands, in addition to the synchronization type.

Tentatively, the results for the coupled Rössler oscillators suggest that the direction of influence can be inferred from the energy ratio as follows. When the energy ratio is close to unity the direction of influence cannot be inferred via this criterion. For weak coupling, $|E(\mathrm{RC}x_1)/E(\mathrm{RC}x_2)| << 1$, due to the large energy in $\mathrm{RC}^{(1,2)}x_2$ and small energy in $\mathrm{RC}^{(1,2)}x_1$, the direction of influence in the first pair is from x_2 to x_1. The opposite direction of influence is obtained for the second pair. As the coupling increases, so does the degree of synchronization, while the energy ratio between the first and second component within each pair increases but is still less than unity; in this case, we can still identify the direction of influence, in the presence of strong coupling — i.e., for synchronization of the (FP) or (FPA) type.

We suppose that increasing the number of coupled oscillators in the system will make the problem much richer and more than two modes will be involved; probably the number of modes is proportional to the number of oscillators. The route to synchronization might still be similar, however: that is, as the coupling between the oscillators increases, more energy will accumulate in the RCs of the oscillatory modes associated with lower frequencies and possibly broader spatial patterns. The whole system will synchronize when most of the energy accumulates in the RC mode obtained by projection onto the lowest pair of ST-EOFs, and the significant eigenvalues will all

merge into one value.

In the following we analyze the synchronization between different climatic records for the last one-to-two centuries, from the North Atlantic, Eastern Mediterranean, North Africa and the Tropical Pacific. The methodology used is the one described so far. In this perspective, the climate system can be interpreted as being represented by a large number of coupled oscillators (Ghil and Childress, 1987; Lorenz, 1991); their significant modes that have similar periods and are found in distinct regions (Ghil et al., 2002a) may then be due to the coupling of such oscillators. We thus test not only (i) the degree of synchronization, but also (ii) the strength of the coupling, by evaluating the ratio $\varepsilon = E(\mathrm{RC}x_1)/E(\mathrm{RC}x_2)$ for a given oscillatory mode of the cross-spectral analysis, and also, albeit tentatively, (iii) the direction of influence.

3. The climatic records

In this section we examine the spectral properties of several climatic records from the Eastern Mediterranean, Ethiopian Plateau, North Atlantic, and Tropical Pacific Ocean. The climate records from the Eastern Mediterranean are instrumental precipitation records from Jerusalem, and tree-ring records from the Golan Heights. The proxy records associated with the Ethiopian Plateau are the high-water records of the Nile River. For the North Atlantic we use the well-known NAO index, and for the Tropical Pacific Ocean the well-known SOI.

3.1. Jerusalem precipitation record

The annual mean precipitation records from Jerusalem cover the 133 years from 1861 to 1994; see Fig. 2c. The records for the years 1861–1964 were compiled by D. Ashbel, and those for 1965–1994 by the Israel Meteorological Service. It is Dan Yakir (Weizmann Institute of Science) who communicated to us these so-far unpublished records.

To concentrate on the interannual periodicities in these precipitation records, as well as in the other records discussed below, we first removed the lowest-frequency components, including the nonlinear trend (Ghil et al., 2002a). In the rainfall records, the three components that fall in this category are (1,2,3), when carrying out the SSA analysis with a window width of $M = 45$ year. Next we applied Monte Carlo SSA (MC-SSA: Allen and Smith, 1996) with a window of $M = 45$ year to the detrended series. Very similar results were obtained with $M = 50$ year (not shown).

The significant ST-EOFs, ordered by decreasing variance captured, along with the associated periods and variances are the following: the pair (1,2) has a period of 3.1 year and a variance of 18%; the pair (3,4) a period of 2.2 year and a variance of 14%; the pair (5,6) a period of 3.8 year and a variance of 13%; the pair (7,8) a period of 14 year and a variance of 10%; and pair (9,10) has a period of 7.8 year and a variance of 7%. We also applied the multi-taper method (MTM; Thomson, 1982; Ghil et al., 2002a) to the detrended time series in order to check the robustness of the peaks identified via SSA. The above frequencies were identified as significant at the 95% level using MTM, besides the period of 14 year, in SSA pair (7,8), which was significant at the level of 90% only. The MTM test was applied with 3 tapers and a spectral resolution of 0.03 cycle/year. In Fig. 3 we show the MC-SSA and MTM spectra, along with the statistical significance of the peaks.

3.2 The tree-ring record from the Golan Heights

The ring-width records of *Quercus Infectoria* (also called Aleppo oak or Cyprus oak) from the Golan Heights extend over 210 years, 1757–1967; see Fig. 2b. This data set is part of an extensive dendrochronological survey carried out in the Golan Heights in 1967 by Yehuda Feliks (the father of this paper's lead author); see Feliks (1968).

SSA was applied to tree-ring records first by Cook et al. (1995). For our record, the nonlinear trend is captured by the first two eigenmodes of the SSA analysis with a 40-year window. The detrended series was analyzed by MC-SSA with the same window width; very similar results were obtained with $M = 50$ year. The significant pairs are: pair (1,2) with a period of 25 year and 37% of the variance; pair (3,4) with a period of 14 year and 20% of the variance; pair (6,7) with a period of 10 year and 12% of the variance; and pair (9,10) with a period of 7.7 year and 6% of the variance. We also applied MTM analysis, with 3 tapers and a spectral resolution of 0.03 cycle/year, to the detrended time series. The above frequencies were all significant at the 99% level.

The significant pairs with dominant periods that are longer than 7 years capture 75% of the variance of the detrended series. This raises the possibility that the trees integrate climatic effects over several years and thus the trees' physiology acts like a low-pass filter on the climatic signals and thus enhances the low-frequency oscillations. The oscillatory modes of 14 years and 7.7 years are also prominent in the Jerusalem precipitation records.

3.3 The Nile River records

Kondrashov et al. (2005; KFG hereafter) studied extensively the high- and low-water records for the Nile River over the 1300-year time span 622 A.D.–1922 A.D. They found periodicities of 2.2, 4.2, 7.2, 12, 19 and 64 year, some of which had already been found and discussed in the abundant literature on these records; please see KFG for a review. For instance, the 2.2- and 4.2-year signals had been attributed to the long-established connection between the Nile River discharge and the ENSO phenomenon in the Indo-Pacific Ocean (Quinn, 1992), Ropelewski and Halpert (1987, 1989), Camberlin (1995), Wang and Eltahir (1998).

KFG's novel and striking result was the clear presence of a 7.2-year signal in the high-water record. These authors hypothesized that the 7.2-year mode demonstrates the extent of the North Atlantic influences, all the way into East Africa's tropical regions, since a 7–8-year peak has been well documented in several oceanic and atmospheric fields extending over the North Atlantic basin (Moron et al., 1998; Wunsch, 1998; Da Costa and Colin de Verdière, 2002; Dijkstra and Ghil, 2005; Simonnet et al., 2005). The research reported in the present paper was largely motivated by the need to examine more closely this hypothesis.

The high-water record corresponds to the maximum height of the flood reached in August–September, when more than 85% of the flow in the Nile River is supplied by the Blue Nile and Atbara River discharges from the Ethiopian Plateau; this plateau reaches altitudes above 2200 m, and the summer monsoonal rainfall over it peaks between June and September (Wang and Eltahir, 1998; Block and Rajagopalan, 2007). Thus, although the Nile's high water stand was measured by the nilometer at Rhoda Island near Cairo, it is a proxy for rainfall over the Ethiopian Plateau. The measurements at Rhoda Island

ceased in 1922, because of the building of the Lower, or Older, Aswan dam at the beginning of the 20th century, to regulate the Nile River flow.

To extend the records studied by KFG, we used existing measurements of the monthly volume flow for the century 1869–1969 at Aswan, provided in the National Center for Atmospheric Research (NCAR) hydrographic datasets; see http://dss.ucar.edu/cgi-bin/rdabrowse?nb=true&c=topic&cv=Hydrosphere. There is a strong correlation between the summer (July–September) volume flow and the high level of the Nile River near Cairo, since 90% of the annual flow is during the summer and most of it is due to the Blue Nile. Thus we can extend the high-water records of the Nile River by using the volume flow for the years after 1922, and up to 1969, when the new dam was built.

The extension of the KFG high-water record to the more recent past is done by linear regression

$$\hat{h} = av + b \,, \qquad (5)$$

where $\hat{h}$ is the dependent variable, namely the high-water record near Cairo, while the independent variable v is the yearly mean volume flow near Aswan. The regression parameters, a = 1.66 and b = –0.83, are found from the overlapping time interval of $h(t)$ and $v(t)$ during the years 1869–1922. During this interval, the correlation between the time series of h and v is 0.93. In Fig. 4a, the observed high-water record and the one estimated according to Eq. (5) are shown for the interval of overlap. The estimated values are clearly quite accurate, and so the high-water record of the Nile at Cairo, extended until 1969 is shown in Fig. 2a. The spectral characteristics of this record (not shown) are

quite similar to those in KFG, with the differences clearly attributable to this record's relative shortness and to climatic changes between the earlier centuries and 1869–1969.

3.4 North Atlantic Oscillation (NAO)

The NAO has been studied extensively over the last two decades (Hurrell et al., 2003), and its strength has been quantified using several indices. We use here the monthly index over the years 1823–2000, as compiled by Jones et al. (1997); see Fig. 2e. This index is the difference between the normalized sea level pressure at Gibraltar and the normalized sea level pressure over Southwestern Iceland. Jones and colleagues used early instrumental data back to 1823. The data set has been modified in November 2000 and the effect of this change is most evident in the summer; see http://www.cru.uea.ac.uk/~timo/projpages/nao_update.htm.

Here we revisit the index using a somewhat different approach, i.e., we apply M-SSA with 12 channels, each channel being the NAO index in a given month of the year: channel 1 is the index for January, channel 2 for February, and so on, while the time step is 1 year. The window width is again $M = 40$ year.

The significant oscillatory modes for this M-SSA analysis have periods of 7.7, 5.5, 4, 3.2 and 2.2 years. Each of these periods is dominant for a subset, or group, of calendar months. The most prominent oscillatory mode has the period of 7.7 year that is familiar from KFG and it appears as the leading reconstructed component, $RC^{(1,2)}$. This mode is prominent in the winter in December, January and February, in summer in August and in fall in October. In the other calendar months, the amplitude of this mode is smaller at least by a factor of three. Rogers (1984), Robertson (2001), Gámiz-Fortis et al. (2002) and Paluˇs and Novotná (2004) also found an oscillation with a period of about

7.7 year in the NAO index. A quasi-biennial component is present in the closely related Arctic Oscillation, constructed from hemispheric sea level pressures, as well (Trenberth and Paolino, 1981; Robertson, 2001).

Below we concentrate mainly on two seasons. For boreal winter, i.e. December-January–February, we use the average index value for these three months, while in summer we use the index value for August.

3.5 Southern Oscillation Index (SOI)

The SOI is based on monthly fluctuations in mean sea level pressure differences between Tahiti and Darwin, and has been studied extensively. We use the monthly index between years 1876–2006, Fig. 2d, as compiled by the Australian Bureau of Meteorology; see http://www.bom.gov.au/climate/current/soi2.shtml.

Here we revisit the index using SSA applied separately to each month with M = 30 and 40 year; the results were found to be almost the same in the two windows. The oscillatory modes that are statistically significant, at the 95% level, can be classified into 4 broad peaks: 6.2–8.2, 4.8–5.6, 3.5 and 2.1–2.8 years. The 2.1–2.8-year band corresponds to the well-known quasi-biennial oscillation (Rasmusson et al., 1990; Jiang et al., 1995a; Paluˇs and Novotná, 2006), while the 4.8–5.6- and 3.5-year peaks are probably identifiable with the low-frequency or quasi-quadrennial oscillation of ENSO (Jiang et al., 1995a; Ghil and Robertson, 2000).

The 7.7-year oscillatory mode is significant during the boreal spring and summer (May–September), while the 5-year mode is prominent during boreal winter, when ENSO typically reaches its peak amplitude, thus potentially masking the 7.7-yr mode. We further analyzed the summer months May–September by applying M-SSA with a

window of M = 40 year. The leading mode $RC^{(1,2)}$, not surprisingly, has a period of 7.7 year. Significant amplitude modulation is observed; the amplitude is large during 1875–1920, and small during 1925–1975. A similar amplitude modulation is also visible in the 7.7-year component of the NAO index (not shown)

4. Synchronized modes

Oscillatory modes with periods around 4, 7–8 and 12–14 years are thus present in the records from the North Atlantic, Eastern Mediterranean, and Ethiopian Plateau. This clustering raises the possibility of teleconnections between the climate variations in these regions. We next examine separately the synchronization of each period between regions to help determine the source region of the oscillatory mode and its role in the dynamics of each region. The method of synchronization analysis was described in section 2. The analysis is applied to the overlapping portion of the two RC time series in question, with each series normalized by its variance in the overlapping part. In the following, we chose the window width M in the M-SSA to be about $N'/3$, where N' is the length of the overlapping portion of the two time series in question.

4.1 Nile and NAO

The overlapping time interval of the extended high Nile records and NAO index is over the years 1825–1971. Since the monsoon rain over the Ethiopian Plateau occurs during the boreal summer, along with the northward seasonal migration of the intertropical convergence zone (ITCZ), we examine here the summer index of the NAO. The 7.7-year oscillation is prominent in the NAO index during the boreal summer only in August.

We apply M-SSA where channel 1 consists of the high-water Nile records and channel 2 of the NAO index for August. The analysis carried out with a window width of $M = 30$ and 40 years gave almost identical results. The significant oscillatory components have periods of 7.6, 4.3, 3.3 and 2 years.

To concentrate on the interannual periodicities, we first removed the trend, as captured by $RC^{(1,2)}$ of the M-SSA analysis with a 35-year window. We then apply M-SSA again to the detrended time series with M = 35 year. The MC-SSA spectrum is shown in Fig. 4b, along with the statistical significance. The resulting leading oscillatory mode $RC^{(1,2)}$ has a period of 4.3 years, and accounts for 17% of the variance of the detrended series (see Fig. 5b).

The mean phase difference, cf. Eq. (2), is 3.11 radian = 2.1 year, and the standard deviation, cf. Eq. (3), is σ = 0.11 radian = 0.96 month. The amplitude correlation, cf. Eq. (4), is 0.92, and so the synchronization is complete, of (FPA) type, with a near phase opposition between the NAO index and Nile flow. The energy ratio $E(RCx_1)/E(RCx_2)$ is ε = 0.97, where x_1 corresponds to the Nile record and x_2 to the NAO index. This ratio is quite close to unity, suggesting that the coupling between the climate systems that trigger the 4.3-year oscillation in the two regions is very strong. Since the energy ratio is about 1, we cannot identify the direction of influence, but physical plausibility clearly tilts towards the NAO being causal.

The second oscillatory mode is represented by $RC^{(6,7)}$, has a period of 7.6 year, and captures 13% of the variance (see Fig. 5a). The mean phase difference is of 2.5 year and is discussed below, while the standard deviation is σ = 0.23 radian = 0.28 year. The amplitude correlation is 0.95, so the synchronization is complete, of (FPA) type. The energy ratio is ε = 0.28, suggesting that the coupling is moderate and that the NAO induces the 7.6-year oscillation in the Nile River. A potential teleconnection mechanism between the climate systems in the two regions that triggers this oscillation is discussed below, in connection with Fig. 7.

The oscillatory mode $RC^{(9.10)}$ has a period of 3.3 year and accounts for 10% of the variance (Fig. 5c). The mean phase difference is 1.37 radian = 0.72 year (discussed below) and the standard deviation $\sigma = 0.42$ radian = 0.22 year. The amplitude correlation is 0.85, so the synchronization is almost complete. However, the ratio $E(RCx_1)/E(RCx_2)$ = 0.11, suggesting that the coupling is very weak.

To explore the teleconnection mechanism between the North Atlantic and the Nile River floods, Fig. 6a shows the mean low-level moisture fluxes during the month of August, computed from the National Centers for Environmental Prediction (NCEP)-NCAR atmospheric reanalyses (Kalnay et al., 1996); the pattern is qualitatively similar throughout the June–September season (not shown). From the figure it follows that the rain over the Ethiopian Plateau is largely a result of moisture flux convergence from the south and north, associated with the northward displacement of the ITCZ. Northward fluxes during boreal summer advect moisture from the equatorial Atlantic, and possibly the Indian Ocean, while the southward flux originates over the eastern Mediterranean.

The Somali jet transports humid air from the western part of the Indian Ocean northwestward, to the eastern slopes of the Ethiopian Plateau, which reach altitudes above 2000 m; this humidity flux is plotted as track 1 in Fig. 6b. As this humid air climbs above the plateau, it cools, condenses and discharges its humidity as rain. However, most of the rain from this source falls over the eastern part of the Plateau and so its role in contributing to the flow of the Blue Nile is limited.

The second track of humid air to the Ethiopian Plateau starts off the equatorial Atlantic Ocean and is associated with the West African monsoon; this moisture flux is limited to the shallow layer beneath the African easterly jet at 700 hPa (Nicholson and

Grist, 2003), and is plotted as track 2 in Fig. 6b. A significant southward flux of moisture from the Mediterranean and Red Sea is visible in Fig. 6a, with some moisture flux divergence over the Eastern Mediterranean; this humidity contribution is shown as track 3 in Fig. 6b. This third track is also found in maps of humidity flux drawn by James (1995, p. 250), Mariotti et al. (2002), and Mohamed et al. (2005). As these air masses reach the northern slopes of the Ethiopian Plateau, they ascend to levels above 3000 m, near the core of the African easterly jet. At these altitudes, the jet transports the ascending air over the Plateau, where it is cooled, condensed and discharges its moisture as rain in the catchment area of the Blue Nile and the Atbara River.

Although most studies on the NAO have focused on the winter season, Folland et al. (2008) have recently studied its summertime expression during July and August. They demonstrate that the NAO's positive phase is associated with anomalously wet conditions over the western Mediterranean, and anomalously dry conditions across the Sahel; see also Hurrell and Folland (2002). Correlation maps (not shown) indicate a broad-scale influence on low-level winds over Africa and the Mediterranean; in its positive phase, the summertime NAO tends to weaken the West African monsoon (described as track 2 above), while tending also to weaken the flow across the Mediterranean and Egypt associated with track 3.

A mean phase difference of 2.5 year in the 7-year oscillation and 2.1 year in the 4.2-year oscillation is found in the coupled oscillatory modes of the NAO index and the Nile records. The almost exact phase opposition at the 4.2-year period indicates that the negative phase of the NAO is associated with enhanced Nile River flow at this period, with the West African monsoon (track 2) most active. For the 7-year period, the delay in

the Nile River flow is closer to a quarter period than to a half-period, and it is thus more likely that the Eastern Mediterranean track 3 plays a greater role at this period.

4.2 The rain in Jerusalem and the NAO index

The 134-year time interval of overlap between the precipitation records in Jerusalem and the NAO index is 1961–1993. Since the rainy season in the eastern part of the Eastern Mediterranean is during the winter months, we use the mean value of the NAO index during December–April in our analysis.

We apply M-SSA with channel 1 consisting of the NAO index and channel 2 of the precipitation record in Jerusalem. The analysis carried out with M = 30 and 40 year gave almost the same results for both values of M. The significant oscillations have periods of 7.8, 3.8, 3.1 and 2 years.

To better study the interannual periodicities we first removed the trend, captured by $RC^{(1)}$ of the M-SSA analysis with a 35-year window. We then applied M-SSA to the detrended time series with M = 35 years. The MC-SSA spectrum, along with the statistical significance, is shown in Fig. 7a.

The leading oscillatory mode, $RC^{(1,2)}$, has a period of 7.8 years, and accounts for 19% of the variance (Fig. 7b). The mean phase difference is – 0.17 radian = – 0.2 year, with a standard deviation of σ = 0.05 radian = 0.06 year. The amplitude correlation is 0.96, and so the synchronization is complete, of (FPA) type. The energy ratio ε in this mode is $E(RCx_1)/E(RCx_2)$ = 2.8, where x_1 corresponds to the NAO index and x_2 to the Jerusalem rainfall, suggesting that the NAO induces the 7.8-year oscillation in Jerusalem rainfall and that the coupling is moderate.

The in-phase relationship between the NAO index and Jerusalem rainfall is consistent with the results of Dunkeloh and Jacobit (2003). In the positive phase of the NAO, higher pressures extend broadly over southern Europe and the Mediterranean, but over the far Eastern Mediterranean surface pressures are lower, with an upper-level trough extending all the way from Iceland. This trough pushes very cold air over the relatively warm Mediterranean Sea, and results in unstable air leading to increased rainfall over the eastern and southeastern rim of the basin.

On the other hand, Eshel and Farrell (2000) claim the opposite for the eastern and southern parts of the Eastern Mediterranean. They found that the correlation between the NAO index and the average precipitation in the whole Eastern Mediterranean is negative. Their conclusion is based on averaging precipitation from the region, but in fact the stations in western Turkey, which are the densest, determine their average precipitation values. Thus the results of Eshel and Farrell (2000) are relevant only to the rainfall in western Turkey, and not to the eastern and southern part of the Eastern Mediterranean, where the effect has the opposite sign.

The oscillatory mode $RC^{(5,6)}$ has a period of 3.1 year, and accounts for 12% of the variance. The mean phase difference is 18.7 radian = 9.2 year, with a standard deviation of σ = 10.6 radian = 5.2 year. The amplitude correlation is 0.29, and so the Eastern Mediterranean and the NAO are not synchronized at this period.

The oscillatory mode $RC^{(7,8)}$ has a period of 3.8 year, and accounts for 11% of the variance (Fig. 7c). The mean phase difference is – 0.27 radian = 0.13 year, and the standard deviation, σ = 0.19 radian = 0.11 year. The amplitude correlation is 0.84, and so the synchronization type is close to (FPA). The energy ratio ε_{78} is $E(RCx_1)/E(RCx_2)$ =

0.8, thus suggesting that the coupling is strong. Since the ratio is close to unity, it does not determine the direction of influence, but physical reasoning again leads us to suspect that the NAO induces this oscillation in the Eastern Mediterranean.

4.3 Tree rings and the NAO index

The 107-year time interval of overlap between the tree-ring record in the Golan Heights and Jerusalem precipitation extends over 1861–1968. We applied M-SSA to this time interval, with channel 1 consisting of the tree-ring widths and channel 2 of Jerusalem precipitation. The analysis was carried out with M = 30 and 40 years, with very similar results in both cases. The significant oscillations have periods of 12.5, 7.8, and 3.8 years.

To better study the interannual periodicities, we first removed the trend, captured by $RC^{(1-4)}$ with M = 30 years. We then applied M-SSA to the detrended time series with the same window width.

The oscillatory mode $RC^{(1,2)}$ has a period of 3.8 years, and accounts for 17% of the variance. The mean phase difference is 0.8 radian = 0.48 year, with standard deviation, σ = 1.23 radian = 0.7 year. The amplitude correlation is 0.77, and so the synchronization type is (FP). The energy ratio ε_{12} is $E(RCx_1)/E(RCx_2)$ = 0.01, where x_1 corresponds to the tree-ring records and x_2 to the Jerusalem precipitation records. This ratio suggests that — while the coupling is quite weak — the rain induces the 3.8-year oscillation in the tree growth, in agreement with intuition.

The oscillatory mode $RC^{(3,4)}$ has a period of 12.5 years, and contains 16% of the variance; it is shown in Fig. 8. The mean phase difference is 1.57 radian = 3.3 year, and the standard deviation, σ = 1.64 radian = 3.26 year. The amplitude correlation is 0.98. It is surprising that the amplitude correlation is very high but the phase is not synchronized,

so we have a synchronization type that was not previously encountered, but can be labeled (FA). The energy ratio is $E(\mathrm{RC}x_1)/E(\mathrm{RC}x_2) = 0.70$. This ratio suggests that the coupling is strong and that the rain induces the 12.5-year oscillation in the tree growth, as expected. The oscillatory mode $\mathrm{RC}^{(11,12)}$ has a period of 7.8-year, and captures 10% of the variance. The mean phase difference is 0.42 radian = 0.5 year, and the standard deviation is $\sigma = 2.47$ radian = 3.07 year. The amplitude correlation is –0.54, and so the synchronization type is (F). The ratio ε_{34} is $E(\mathrm{RC}x_1)/E(\mathrm{RC}x_2) = 0.41$, suggesting that the coupling is moderate rain and that the rainfall induces the 7.8-year oscillation in the tree-ring record as well.

It might appear somewhat surprising that the synchronization between the rainfall records in Jerusalem and the tree-ring records in the Golan Heights has such a relatively weak degree of synchronization. Two main climatic factors determine tree growth: the amount of rain and the temperature. Usually more rain causes larger tree-ring growth, while cool winters result in less growth. Since the rainy winters are also cooler in the Eastern Mediterranean, these two factors have an opposing effect on the tree growth, thus tending to weaken the rainfall signal in the tree-ring record.

4.4 The Southern Oscillation, NAO and the Nile River

The 124-year interval of overlap between the extended SOI and the NAO index is 1876–1999. First we examined the mean index of the winter months, December–April, and applied M-SSA with channel 1 consisting of the SOI and channel 2 of the NAO index. The analysis was carried out with both $M = 30$ and 40 years, and the results were almost the same in both cases. The only significant oscillatory mode common to the 2 indices has a period of 3.8 year and is captured by $\mathrm{RC}^{(3,4)}$. The mean phase difference is 22.6

radian = 13.7 year, and the standard deviation is σ = 14.2 radian = 8.6 years. The amplitude correlation is 0.31, and so the two time series are not synchronized. We thus conclude that there is no teleconnection between the two regions in boreal winter.

Because the 7.7-year oscillation is prominent in the SOI in boreal summer and in the NAO index in August, we applied M-SSA with a window width of M = 30 year, where channel 1 consists of the SOI and channel 2 is the NAO index, both for the calendar month of August. The MC-SSA spectrum, along with the statistical significance, is shown in Fig. 9a. The leading oscillatory mode is $RC^{(1,2)}$; it has a period of 7.2 year, contains 9% of the variance, and it is plotted in Fig. 9b.

The mean of the phase difference is 2.6 radians = 3 years, and the standard deviation is σ = 0.21 radians = 0.25 years. The amplitude correlation is 0.96, and so the synchronization type is (FPA). The ratio $E(RCx_1)/E(RCx_2)$ = 0.83, where x_1 corresponds to the SOI record and x_2 to the NAO index. This ratio suggests that the coupling is strong and that the NAO induces the 7.7-year oscillatory mode in the SOI.

The oscillatory mode $RC^{(4,5)}$ has a period of 3.7 years, and contains 6% of the variance. The mean phase difference is 1.88 radian = 1.1 year, and the standard deviation σ = 1.61 radian = 0.9 year. The amplitude correlation is 0.83, and so the synchronization type is again (FA). The energy ratio ε_{45} is $E(RCx_1)/E(RCx_2)$ = 5.3, suggesting that the Tropical Pacific Ocean induces this oscillation in the North Atlantic, but the coupling between the two regions in this frequency band is very weak.

The 95-year interval of overlap between the SOI and the extended Nile River series is between 1876 and 1971. Since the monsoon rains over the Ethiopian Plateau occur during the boreal summer, we examine here the SOI index for the summer months

July–September. We applied M-SSA to the two time series, with a window of M = 35 year. The MC-SSA spectrum, with the statistical significance, is shown in Fig. 10a.

The joint oscillatory mode $RC^{(1,2)}$ has a period of 7.5 year, and it represents 10% of the variance; it is plotted in Fig. 10b. The mean phase difference is 0.39 radian = 0.47 year, and the standard deviation is σ = 0.32 radian = 0.38 year. The amplitude correlation is 0.97, and so the synchronization is complete, of (FPA) type. The ratio ε_{12} is $E(RCx_1)/E(RCx_2)$ = 1.64, where x_1 corresponds to the SOI and x_2 to the Nile River record. This ratio suggests that the coupling between the two regions is moderate.

We showed above (in sections 4.1 and this one) that the 7–8-year oscillatory mode in the Nile River high-water record and the SOI may be induced by the NAO; on the other hand, the current result suggests that this oscillation in the Nile River floods might also be affected by the Southern Oscillation, acting as a mediator. The impact of ENSO extends across the Sahel, and has been attributed to large-scale tropospheric temperature increases and the resulting stabilization of the atmospheric column, which tends to decrease the moisture flux convergence into the ITCZ from all sources (Giannini et al., 2005; Chiang and Sobel, 2002; Lintner and Chiang, 2007).

The oscillatory mode $RC^{(6,7)}$ has a period of 3.7 year, and it captures 8% of the variance; it is shown in Fig. 10c. The mean phase difference is –0.2 radian = –0.12 year, and the standard deviation is σ = 0.5 radian = 0.3 year, while the amplitude correlation is –0.53; the synchronization type, therewith, is (FP). The ratio ε_{67} is $E(RCx_1)/E(RCx_2)$ = 1.39 and thus consistent with coupling being strong and with this mode being induced by the quasi-quadrennial oscillation in ENSO.

5. Concluding remarks

5.1 Summary

Evidence for oscillatory modes of variability over the North Atlantic, Ethiopian Plateau, Eastern Mediterranean and the Tropical Pacific Ocean was examined using climate records from each region: the NAO index for the North Atlantic, Nile River high-water records for the Ethiopian Plateau, the precipitation in Jerusalem and a tree-ring record from the Golan Heights for the Eastern Mediterranean, and the SOI for the Tropical Pacific Ocean.

Statistically significant oscillatory modes — having periods of about 4 and 7–8 years — were identified in all records. This clustering of periodicities raises the possibility of teleconnections between these regions (Ghil et al., 2002a). Other significant oscillatory modes were found in some of the records only: a mode with a period of 14 year in Jerusalem rainfall and tree rings, and one with 3.3 year in the NAO index and high-water Nile record.

The 7–8-year mode was found to be prominent in our indices during December–February, August and October. It might be induced by an oscillation of similar period in the position and strength of the Gulf Stream's sea surface temperature (SST) front in the North Atlantic, identified in previous studies (Deser and Blackman, 1993; Joyce et al., 2000; Feliks et al., 2004; Dijkstra and Ghil, 2005; Simonnet et al., 2005). We shall return to this hypothesis in the next subsection.

We have approached climatic teleconnections between regions in terms of synchronization of chaotic oscillators. Our approach is based, on the one hand, on the work of J. Kurths and colleagues (Rosenblum et al., 1996; Osipov et al., 2003) and, on

the other, on pre-filtering and spectral analysis of the time series of interest, via singular-spectrum analysis (SSA) and multi-channel SSA (M-SSA). In addition, we examined the strength of the coupling and the direction of influence by examining the energy (or variance) ratio between various channels, in separate frequency bands identified by the M-SSA.

The methodology was presented in section 2, and illustrated by its application to the two coupled Rössler oscillators previously used by Rosenblum (1996). As the coupling between the oscillators increases, their time series synchronize, first in frequency (F), then in phase (FP), and finally in amplitude as well (FPA). In addition to following these steps in the synchronization, as defined by Osipov et al. (2003), we study the route to synchronization by examining the joint spectra of the oscillatory modes, using a two-channel M-SSA. For the two coupled Rössler oscillators, the strength of the coupling can be measured, without explicit reference to the value of the coupling constant C, cf. Eqs. (5), by examining the ratio $\varepsilon_{k,k+1}$ of the energy (or variance) in the two channels of the reconstructed components (RCs) of the oscillatory mode (k, k + 1) under study. As the coupling between the two oscillators increases, the energy ratio tends to unity and the energy accumulates in a single oscillatory mode.

We apply the above method to examine the synchronization between our climatic time series, based on the broad theoretical concept that the climate system can be described as a large, or even infinite, number of coupled oscillators, as discussed at the end of section 2; see also Ghil and Childress (1987) and Lorenz (1991). Our hypothesis is that the commonality between several oscillatory modes found in the set of climate indices analyzed is due to the coupling between the oscillators. The significant oscillatory

modes of the joint spectra of the climate records studied here, their synchronization type, and the energy ratio in each mode are summarized in Table 2.

The 7–8-year oscillatory mode in all the regions is completely synchronized, of (FPA) type, and the energy analysis suggests that the NAO induces this mode in the other regions; we refer again to the next subsection for further discussion of the possible origin of this mode in the North Atlantic. The boreal-summer teleconnection between the NAO and the Ethiopian Plateau's rainfall, as captured by the Nile River high-water record, is likely to involve the NAO's influence on the West African monsoon (Folland et al., 2008). Our results suggest that the SOI, acting as a mediator, may also contribute to the 7–8-year oscillation in the Ethiopian Plateau's climate; this effect may be related to the strong impact of ENSO on Ethiopian summer rainfall through changes in tropospheric stability (Giannini et al., 2005; Chiang and Sobel, 2002; Lintner and Chiang, 2007).

The coupling in the 7.2-year oscillatory mode of the joint spectra between the North Atlantic and Tropical Pacific Ocean is very strong, and its mechanism is plausibly based on previous studies. Chiang and Vimont (2003) have shown evidence that the extratropical atmosphere can influence the tropical Pacific through a meridional mode, analogous to that in the tropical Atlantic, in which variations in the trade winds in the northern subtropics influence tropical SSTs. Thompson and Lorenz (2004) have identified relationships between the extratropical annular modes and circulation in the tropical troposphere.

An (FPA)-type synchronization at 7.8 year is also found between the North Atlantic and the eastern part of the Eastern Mediterranean during winter, which is the rainy season in the latter region; this teleconnection can be explained using the results of

Dunkeloh and Jacobit (2003). These authors showed that, during the winter, a low-pressure anomaly extends from Northern Europe to the southern and eastern part of the Eastern Mediterranean. The NAO index determines the strength of this low-pressure anomaly and, therewith, the amount of rain in the eastern and southern part of the Eastern Mediterranean.

An oscillatory mode with a period of about 4 years is found in all our climate records as well. A teleconnection to the Ethiopian Plateau, related to the quasi-quadrennial (or low-frequency) ENSO mode (Rasmusson et al., 1991; Jiang et al., 1995a) has been the subject of several studies (e.g., Giannini et al., 2005; Chiang and Sobel, 2002; Lintner and Chiang, 2007); it appears to be associated with ENSO influence on changes in tropospheric static stability that affect convection over Ethiopia. There is no evidence that this mode in the NAO and the Eastern Mediterranean is induced by ENSO, since the energy ratio in the joint M-SSA spectra of the NAO index and SOI is very small, $\varepsilon = 0.1$.

On the other hand, the energy ratio in the two-channel, 4-year M-SSA mode for the NAO index and Jerusalem rainfall is $\varepsilon = 0.8$. We suggest that this mode may be induced in the North Atlantic climate by a 4-year oscillation (possibly a harmonic of the 7–8-year oscillation) of the position of the Gulf Stream SST front. In the joint spectra of the Nile record and the NAO index, a 4.2-year oscillatory mode is also prominent. The synchronization type of this mode is (FPA), and the coupling between the two regions is very strong, with an energy ratio of $\varepsilon = 0.97$. Thus the Ethiopian Plateau appears to exhibit independent teleconnections with both the North Atlantic and ENSO, at a period of about 4 years.

In the Eastern Mediterranean, an oscillatory mode with a period of about 14 years is prominent in the Jerusalem rainfall record and in tree rings from the Golan Heights. The oscillatory mode of the joint spectral analysis for the rainfall and tree rings has a period of 12.5 years. Although the coupling between the rainfall record and the tree rings is relatively strong, the synchronization type is of (FA) type. This type is differs from the three types introduced by Osipov et al. (2003) — which were also the ones we found useful in other two-channel M-SSA analyses here — series since the amplitudes are well correlated, while the phases are not synchronized.

We attribute this unusual result to the physiology of tree-ring growth. Two principal climatic factors determine this growth, namely rainfall and temperature. In the Eastern Mediterranean, rainy winters are also cooler so these two factors have a tendency to cancel out. In the tree-rings record, the significant periods that are longer than 7 years capture 75% of the variance of the detrended time series. This raises the possibility that the trees' physiology acts like low-pass filter on the climatic signals.

5.2 Discussion

This work grew out of Kondrashov et al. (2005) finding a 7–8-year oscillation in a 1300-year long record of Nile River water levels. Searching for the sources of the Nile has been a multi-millennial quest, starting with up-river military expeditions of the pharaohs, to find and protect the headwaters of the Nile, continuing with the quest for the mythical Prester John in the Middle Ages, and only ending in the 19th century, with the European expeditions that finally reached the sources of the White and Blue Nile. Likewise, the search for the explanation of Joseph's dream about the alternation of seven fat and seven lean years goes back several thousand years and might not be over yet.

We wish to examine further the 7–8-year mode, which plays such a prominent role in the NAO and in the regions that are teleconnected to it, and to verify the hypothesis that this mode arises from an oscillation of similar period in the meridional position and intensity of the Gulf Stream's SST front. Such an oscillation was identified in previous studies of atmospheric and oceanic fields over the North Atlantic basin (Deser and Blackmon, 1993; Moron et al., 1998; Joyce et al., 2000; Da Costa and Colin de Verdière, 2002; Dijkstra and Ghil, 2005; Simonnet et al., 2005).

To proceed with this verification, we analyzed western-North-Atlantic data from the Simple Ocean Data Assimilation (SODA) reanalysis (Carton and Giese, 2008), over the rectangular domain (32^0N–43.5^0N, 75^0W-50^0W). The choice of this limited domain of the Gulf Stream and associated recirculation gyres is justified by the previously mentioned work on the gyre mode and its 7–8-year periodicity (Jiang et al., 1995b; Speich et al., 1995; Simonnet et al., 2003a, b, 2005; Dijkstra and Ghil, 2005; Simonnet, 2005) and by the findings of Wang et al. (2004), who showed that it is the Gulf Stream region alone that affects the NAO. Feliks et al. (2004, 2007) demonstrated the impact of a narrow and vigorous SST front, like the Gulf Stream front, on the atmosphere above and downstream, while Minobe et al. (2008) carried out calculations along these lines in a high-resolution general circulation model of the global atmosphere, with realistic SST forcing, and compared their results with satellite observations.

We present here preliminary results using the mean-monthly data from SODA for the sea surface temperature (SST) and sea surface height (SSH) fields for the 50-year interval 1958–2007; the SSH field corresponds to the barotropic flow component. The mean SST field in the central panel of Fig. 11 and the mean SSH field in the central panel

of Fig. 12 show a strong SST front aligned with the Florida Current, which flows along the East Coast until the separation point at Cape Hatteras.

We applied M-SSA to the SSH data with a window width of $M = 200$ month. The leading oscillatory mode is captured by $RC^{(1,2)}$, has a period of 1 year, and contains 12% of the variance. The second oscillatory mode, $RC^{(3,4)}$, has a period of 8.5 years and contains 5% of the variance. This oscillatory mode is shown in Fig. 13 at the point (73 ^{0}W, 37.5 ^{0}N), where its maximum amplitude is reached. The 8.5-year oscillation (red curve) captures quite well the interannual variability of the raw data (black curve).

Phase composites of the 8.5-year mode are shown in Fig. 11 for the SST field and in Fig. 12 for the SSH field, by dividing the oscillation into eight phase categories, according to the methodology of Moron et al. (1998, see their appendix for details). This oscillatory mode captures the interannual, as distinct from the seasonal, north- and southward motions of the mean Gulf Stream path, downstream of the separation point. Feliks et al. (2004, 2007) studied the impact of this oscillation on the overlying atmosphere, and further work on this topic is under way.

The spatio-temporal structure of the 8.5-year mode, as shown in Figs. 11 and 12, shares certain features with the so-called gyre mode found in several oceanic models (Jiang et al., 1995b; Speich et al., 1995; Ghil et al., 2002b; Simonnet et al., 2003a, b, 2005; Dijkstra and Ghil, 2005; Simonnet, 2005), on the one hand, and with the NAO, on the other (Moron et al., 1998; Da Costa and Colin de Verdière, 2002; Dijkstra and Ghil, 2005; Simonnet et al., 2005). In the simple and intermediate models, the oceanic basin was rectangular and the fluxes at the sea surface were idealized functions of time and space, while the observational studies concentrated thus far on atmospheric or SST data

sets. The availability of SODA will allow us to examine these issues in greater detail in a separate publication.

The evidence presented here for oscillatory climate modes with planetary-scale teleconnections may have implications for prediction, especially at lead times beyond seasonal ones, for which dynamical models are not yet used. Robertson et al. (2001) demonstrated river-flow predictability up to 4 years in advance for low-flow years on the Paraná River in southeastern South America. The predictions were based on an 8-year periodicity in the river flow time series identified using SSA. Robertson and Mechoso (1998) found this periodicity to be related to SST anomalies in the tropical North Atlantic. Further work is required to relate these findings to those of the present paper.

Acknowledgements. It is a pleasure to thank D. Yakir for the precipitation records from Jerusalem, A. Zukerman for digitizing the tree rings graphs, and many colleagues for useful discussions. Among the latter, G. Duane, A. Groth, J. Kurths and J.J. Tribbia played a role in familiarizing us with the literature on synchronization of chaotic oscillators. This work was supported by U.S. Department of Energy grant DE-FG02-07ER64439 from its Climate Change Prediction Program, and by the European Commission's No. 12975 (NEST) project "Extreme Events: Causes and Consequences (E2-C2)."

References

Allen, M. R., and A. W. Robertson, 1996: Distinguishing modulated oscillations from colored noise in multivariate datasets. *Climate Dyn.,* **12**: 775–784.

Allen, M. R., and L. A. Smith, 1996: Monte Carlo SSA: Detecting irregular oscillations in the presence of coloured noise, *J. Clim*., **9**, 3373–3404.

Barnston A. G., and R. E. Livezey, 1987: Classification, seasonality and persistence of low-frequency atmospheric circulation patterns. *Mon. Wea. Rev*, **115**, 1083–1126.

Block, P., and B. Rajagopalan, 2007: Interannual variability and ensemble forecast of upper Blue Nile basin seasonal precipitation. *J. Hydrometeor*., **8,** 327–343.

Broomhead, D.S., and G.P. King, 1986a: Extracting qualitative dynamics from experimental data. *Physica D*, **20**, 217–236.

Broomhead, D. S., and G. P. King, 1986b: On the qualitative analysis of experimental dynamical systems, in *Nonlinear Phenomena and Chaos*, edited by S. Sarkar, pp. 113–144, Adam Hilger, Bristol, England.

Camberlin, P., 1995: June–September rainfall in north-eastern Africa and atmospheric signals over the tropics: A zonal perspective. *Int. J. Climatol.,* **15,** 773–783.

Carton, J. A. and B. S. Giese, 2008: A reanalysis of ocean climate using Simple Ocean Data Assimilation (SODA). *Mon. Wea. Rev.*, **136**, 2999–3017.

Chao, Y., M. Ghil, and J. C. McWilliams, 2000: Pacific interdecadal variability in this century's sea surface temperatures, *Geophys. Res. Lett*., **27**, 2261–2264.

Chiang, J. C. H., and A. H. Sobel, 2002: Tropical tropospheric temperature variations caused by ENSO and their influence on the remote tropical climate. *J. Climate*, **15**, 2616–2631.

Chiang, J. C. H., and D. Vimont, 2004: Analogous Pacific and Atlantic meridional modes of tropical atmosphere-ocean variability. *J. Climate*, **17**, 4143–4158.

Cook, E. R., B. M. Buckley, and R. D. D'Arrigo, Interdecadal temperature oscillations in the Southern Hemisphere, 1995: Evidence from Tasmanian tree rings since 300 B. C., in *Natural Climate Variability on Decade-to-Century Time-Scales*, edited by D. G. Martinson *et al*., pp. 523–532, National Academies Press, Washington, D. C.
Da Costa, E. D., and A. Colin de Verdière, 2002 : The 7.7-year North Atlantic oscillation, *Q. J. R. Meteorol. Soc*., **128A**, 797–817.

Deser, C., and M. L. Blackman, 1993: Surface climate variation over the North Atlantic Ocean during winter: 1900–1999, *J. Clim.,* **6**, 1743–1753.

Dettinger, M. D., M. Ghil and C. L. Keppenne, 1995: Interannual and interdecadal variability in United States surface-air temperatures, 1910–87, *Climatic Change*, **31**, 35–66.

Dijkstra, H.A., and M. Ghil, 2005: Low-frequency variability of the large-scale ocean circulation: A dynamical systems approach, *Rev. Geophys*., RG3002, doi:10.1029/2002RG000122.

Duane, G.S., 1997: Synchronized chaos in extended systems and meteorological teleconnections, *Phys. Rev. E*, **56**, 6475–6493.

Duane, G.S., and J.J. Tribbia, 2004: Weak Atlantic–Pacific teleconnections as synchronized chaos, *J. Atmos. Sci*., **61**, 2149–2168.

Dunkeloh, A. and J. Jacobvit, 2003: CIirculation dynamics of MEDITERRANEAN precipitation variability 1948–98. *Int. J. Climatol*. **23**: 1843–1866

Eshel, G., and B. F. Farrel, 2000: Mechanisms of eastern Mediterranean rainfall variability. *J. Atmos. Sci*., **57**, 3219–3232.

Feliks, Y., 1968: Tree and forest in the Golan Heights. *Teva Vaeretz*, 3–16 (in Hebrew).

Feliks, Y., M. Ghil and E. Simonnet, 2004: Low-frequency variability in the midlatitude atmosphere induced by an oceanic thermal front. *J. Atmos. Sci.,* **61,** 961–981.

Feliks, Y., M. Ghil, and E. Simonnet, 2007: Low-frequency variability in the mid-latitude baroclinic atmosphere induced by an oceanic thermal front, *J. Atmos. Sci*., **64**, 97–116.

Folland C. K., J. Knight, H. W. Linderholm, D. Fereday, S. Ineson, and J. W. Hurrell, 2008: The Summer North Atlantic Oscillation: past, present and future**.** *J. Climate*. (in press)

Gabor, D., 1946: Theory of communication. *J. IEE* (London), **93**, 429–457.

Gámiz-Fortis, S. R., D. Pozo-Vázques, M.J. Esteban-Parra, and Y. Castro-Díez: Spectral characteristics and predictability of the NAO assessed through Singular Spectral Analysis, *J. Geophys. Res*., **107**, D23:4685, 2002.

Ghil, M., and Childress S., 1987: *Topics in Geophysical Fluid Dynamics: Atmospheric Dynamics, Dynamo Theory and Climate Dynamics*, Springer-Verlag, New York/Berlin/London/Paris/ Tokyo, 485 pp.

Ghil, M., and A. W. Robertson, 2000: Solving problems with GCMs: General circulation models and their role in the climate modeling hierarchy. *General Circulation Model Development: Past, Present and Future,* D. Randall (Ed.), Academic Press, San Diego, pp. 285–325.

Ghil, M., M. R. Allen, M. D. Dettinger, K. Ide, D. Kondrashov, M. E. Mann, A. W. Robertson, A. Saunders, Y. Tian, F. Varadi, and P. Yiou, 2002a: Advanced spectral methods for climatic time series*, Rev. Geophys*., **40**(1), pp. **3**.1–**3**.41, doi: 10.1029/2000RG000092.

Ghil, M., Y. Feliks, and L. Sushama, 2002b: Baroclinic and barotropic aspects of the wind-driven ocean circulation, *Physica D*, 167, 1–35.

Giannini, A., R. Saravanan, and P. Chang, 2005: Dynamics of the boreal summer African monsoon in the NSIPP1 atmospheric model. *Climate Dyn.,* **25***,* 517–535.

Hasegawa, T., and T. Torii, 1991: An automatic quadrature for Cauchy Principal Value integrals, *Math. Comput*., **56**, 741–754.

Henrici, P., 1963: *Error Propagation for Difference Methods*, J. Wiley, New York/London, 73 pp.

Hurrell, J.W., 1995: Decadal trends in the North Atlantic Oscillation: Regional temperatures and precipitation, *Science*, **269**, 676–679.

Hurrell, J.W., and C.K. Folland, 2002: A Change in the Summer Atmospheric Circulation over the North Atlantic. *CLIVAR Exchanges*, Vol. 25, pp. 52-54.

Hurrell, J. W., Y. Kushnir, G. Ottersen, and M. Visbeck, 2003: An overview of the North Atlantic Oscillation. *The North Atlantic Oscillation: Climatic Significance and Environmental Impact, Geophys. Monogr.,* Vol. 134, American Geophysical Union, pp. 1–35.

Isaacson, E., and H. B. Keller, 1966: *Analysis of Numerical Methods*, J. Wiley, New York/London/Sydney, 541 pp.

James, I. N., 1995: *Introduction to Circulating Atmospheres*, Cambridge University Press, Cambridge, 422 pp.

Janjarasjitt, S., and K.A. Loparo, 2008: An approach for characterizing coupling in dynamical systems, *Physica D*, **237**, 2482–2486, doi:10.1016/j.physd.2008.03.003

Jiang, N., J. D. Neelin and M. Ghil, 1995a: Quasi-quadrennial and quasi-biennial variability in the equatorial Pacific. *Clim. Dyn.*, **12**, 101–112.

Jiang, S., F.-F. Jin, and M. Ghil, 1995b: Multiple equilibria, periodic, and aperiodic solutions in a wind-driven, double-gyre, shallow-water model, *J. Phys. Oceanogr.*, **25**, 764–786.

Jones, P.D., T. Jonsson, and D. Wheeler, 1997: Extension to the North Atlantic Oscillation using early instrumental pressure observations from Gibraltar and South-West Iceland. *Int. J. Climatol.* **17**, 1433–1450.

Joyce, M. T., C. Deser and M. A. Spall, 2000: The relation between decadal variability of subtropical mode water and the North Atlantic Oscillation. *J. Climate*, **13**, 2550–2569.

Keppenne, C. L., and M. Ghil, 1993: Adaptive filtering and prediction of noisy multivariate signals: An application to subannual variability in atmospheric angular momentum, *Intl. J. Bifurcation & Chaos*, **3**, 625–634.

Kondrashov, D., Y. Feliks, and M. Ghil, 2005: Oscillatory modes of extended Nile River records (A.D. 622–1922), *Geophys. Res. Lett.*, **32***,* L10702, doi:10.1029/2004GL022156.

Lintner, B. R., and J. C. H. Chiang, 2007. Adjustment of the remote tropical climate to El Niño conditions. *J. Climate*, **20**, 2544-2557.

Lorenz, E. N., 1963: Deterministic nonperiodic flow. *J. Atmos. Sci.*, **20**, 130–141.

Lorenz, E.N., 1991: Dimension of weather and climate attractors, *Nature*, **353**, 241–244.

Maloney, E. D. and J. Shaman, 2008: Intraseasonal variability of the West African monsoon and Atlantic ITCZ. J. Climate, 21, 2898–2918.

Mantua, N.J., S. R. Hare, Y. Zhang, J. M. Wallace, and R.C. Francis, 1997: A Pacific interdecadal climate oscillation with impacts on salmon production, *Bull. Amer. Meteorol. Soc*., **78**, 1069–1079.

Maraun, D., and J. Kurths, 2004: Cross wavelet analysis: significance testing and pitfalls, *Nonlin. Processes Geophys*., **11**, 505–514.

Mariotti, A., M. V. Struglia, N. Zeng and K.-M. Lau, 2002: The hydrological cycle in the Mediterranean region and implications for water budget on the Mediterranean Sea. *J. Climate*, **15**,16741690.

Minobe, S., A. Kuwano-Yoshida, N. Komori, S.-P. Xie, and R.J. Small, 2008: Influence of the Gulf Stream on the troposphere. *Nature*, **452**, doi:10.1038/nature06690.

Mohamed, Y. A., B. J. J. van den Hurk, H. H. G. Savenije and W. G. M. Bastiaanssen, 2005: Hydroclimatology of the Nile: Results from a regional climate model. *Hydrol. Earth System Sci*., **9**, 263278.

Moron, V., R. Vautard, and M. Ghil, 1998: Trends, interdecadal and interannual oscillations in global sea-surface temperatures, *Clim. Dyn.*, **14**, 545–569.

Nicholson, S. E., and J. P. Grist, 2003: The seasonal evolution of the atmospheric

circulation over West Africa and Equatorial Africa. *J. Climate*, **16**, 1013–1030.

Osipov, G.V., B. Hu, C. Zhou, M.V. Ivanchenko, and J. Kurths, 2003: Three types of transitions to phase synchronization in coupled chaotic oscillators, *Phys. Rev. Lett*., **91**, doi: 10.1103/PhysRevLett.91.024101.

Paluˇs, M. and D. Novotná, 2004: Enhanced Monte Carlo Singular System Analysis and detection of period 7.8 years oscillatory modes in the monthly NAO index and temperature records, *Nonlin. Processes Geophys*., **11**, 721–729.

Paluˇs, M. and D. Novotná, 2006: Quasi-biennial oscillations extracted from the monthly NAO index and temperature records are phase-synchronized. *Nonlin. Processes Geophys*., **13**, 287–296.

Panter, P., 1965: *Modulation, Noise, and Spectral Analysis*. McGraw-Hill, New York.

Philander, S. G. H., 1990: *El Niño, La Niña, and the Southern Oscillation*, Academic Press, San Diego, 293 pp.

Plaut, G., and R. Vautard, 1994: Spells of low-frequency oscillations and weather regimes in the Northern Hemisphere. *J. Atmos. Sci.,* **51,** 210–236.

Pozo-Vázques, D., Esteban-Parra, M. J., Rodrigo, F. S., and Castro-Díez, Y. , 2001: A study of NAO variability and its possible nonlinear influence on European surface temperature, *Clim. Dyn*., 17, 701–715.

Rasmusson, E.M., and T.H. Carpenter, 1982: Variations in tropical sea surface temperature and surface wind fields associated with the Southern Oscillation/El Niño, *Mon. Wea. Rev.*, **110**, 354–384.

Rasmusson, E.M., X. Wang, and C.F. Ropelewski, 1990: The biennial component of ENSO variability. *J. Marine Syst.*, **1**, 71–96.

Robertson, A. W., 2001: On the influence of ocean-atmosphere interaction on the Arctic Oscillation in two general circulation models. *J. Climate,* **14**, 3240–3254.

Robertson, A. W., and C. R. Mechoso, 1998: Interannual and decadal cycles in river flows of southeastern South America. *J. Climate,* **11**, 2570–2581.

Robertson, A. W., C. R. Mechoso, and N. O. Garcia, 2001: Interannual prediction of the Parana River. *Geophys. Res. Lett*., **28**, 4235–4238.

Rogers, J. C., 1984: The association between the North Atlantic oscillation and the Southern Oscillation in the Northern Hemisphere. *Mon. Wea. Rev.,* **112**, 1999–2015.

Rogers J. C., 1990: Patterns of low-frequency monthly sea-level pressure variability (1899–1986) and associated wave cyclone frequencies. *J. Climate*, **3**, 1364-1379.

Ropelewski, C. F., and M. S. Halpert, 1987: Global and regional scale precipitation patterns associated with the El Niño/Southern Oscillation. *Mon. Wea. Rev.,* **115,** 1606–1626.

Ropelewski, C.F., and M.S. Halpert, 1989: Precipitation patterns associated with the high-index phase of the Southern Oscillation. *J. Climate,* **2,** 268–284

Ropelewski, C.F., and P.D. Jones, 1987: An extension of the Tahiti-Darwin Southern Oscillation Index. *Mon. Weather Rev.*, **115**, 2161–2165.

Rosen, D., and D.E. Cormack, 1995: The continuation approach: A general framework for the analysis and evaluation of singular and near-singular integrals, *SIAM J. Appl. Math*., 55, 723–762.

Rosenblum, M. G., A.S. Pikovsky, and J. Kurths, 1996: Phase synchronization of chaotic oscillators, *Phys. Rev. Lett*., **76**, 1804–1807.

Simonnet, E., M. Ghil, and H. A. Dijkstra, 2005: Homoclinic bifurcations in the quasi-geostrophic double-gyre circulation, *J. Mar. Res*., **63**, 931–956.

Suselj and Bergant (2006) dealing with MOI indicate that the correlation between MOI and NAOI and PRC (precipitation anomalies is negative above all Mediterranean region. Geophysical Res. Abstract, 8, 02145, Sref-ID:1607-7962/gra/EGU06-A-02145.

Thompson, D. W. J, and D. W. Lorenz, 2004: The signature of the annular modes in the tropical troposphere. *J. Climate,* **17,** 4330-4342.

Trenberth, K. E., and D. A. Paolino Jr., 1981: Characteristic patterns of variability of sea level pressure in the Northern Hemisphere. *Mon. Wea. Rev*., **109**, 1169–1189.

Unal, Y. S., and M. Ghil, 1995: Interannual and interdecadal oscillation patterns in sea level, *Climate Dyn.*, **11**, 255–278.

Walker, G., 1931: On periodicity in series of related terms. *Proc. Roy. Soc. (London) Ser. A*, **131**, 518–532.

Walker, G. T., and E. W. Bliss, 1932: World Weather V. *Mem. Roy. Meteor. Soc.*, **4**, 53–84.

Walker, G. T., and E. W. Bliss, 1937: World Weather VI. *Mem. Roy. Meteor. Soc.*, **4,** No.

39, 119–139.

Wallace, J. M., and D. S. Gutzler, 1981: Teleconnections in the geopotential height field during the Northern-Hemisphere winter. *Mon. Wea. Rev.*, **109**, 784–812.

Wang, G., and E. A. B. Eltahir, 1999. Use of ENSO information for medium- and long-range forecasting of the Nile floods. *J. Climate*, **12**, 1726–1737.

Wang, W., B. T. Anderson, R. K. Kaufmann, and R. B. Myneni, 2004: The Relation between the North Atlantic Oscillation and SSTs in the North Atlantic Basin. *J. Climate*, 17, 4752-4759.

Wunsch, C., 1999: The interpretation of short climate records, with comments on the North Atlantic and Southern Oscillations, *Bull. Am. Meteorol. Soc*., **80**, 245–255.

List of Figures

nilometer record at Rhoda Island, normalized by its maximum of 4.45 m (solid line) and the estimated high-water record — derived by linear regression, cf. Eq. (5) — from the mean annual volume flow measured at Aswan (dashed line); shown for the time interval of overlap, 1869–1922. (b) The two-channel M-SSA spectrum of the extended and detrended Nile River record (channel 1) and the NAO index for the month of August, together with a Monte Carlo significance test for the oscillations; same procedure and conventions as in Fig. 3a, except variances in black.

FIG. 5: The RC pairs that capture the oscillatory modes of the two-channel M-SSA for the Nile River record and the NAO index. The header of each panel is the period of the mode, in decreasing order of period length; channel 1 = Nile River (solid line), channel 2 = NAO index (dashed line).

FIG. 6: Humidity supply tracks leading to the Ethiopian Plateau during summer. (a) Climatological mean map of moisture fluxes and divergence for the month of August, showing vectors of humidity fluxes averaged over the 1000–850 hPa layer, together with the flux divergence (shaded, mm/day), constructed from daily NCEP-NCAR reanalysis data, over the interval 1950–2007. (b) Schematic diagram of the three moisture tracks, labeled in the circles placed at track initiation from (1) to (3).

FIG. 7: Synchronization study of the NAO index (channel 1) and Jerusalem rainfall (channel 2). (a) The M-SSA spectrum of the detrended NAO index and Jerusalem precipitation data, along with the Monte Carlo significance test for the oscillatory modes. (b) The reconstruction of the 7.8-year mode of the M-SSA; NAO index (solid), Jerusalem rainfall (dashed). (c) Same as panel (b), for the 3.8-year mode.

FIG. 8: The RC of the 12.5-year oscillatory mode of the joint spectra between the tree

rings and Jerusalem rainfall; tree rings (solid), Jerusalem rainfall (dashed).

FIG. 9: Synchronization study of the SOI (channel 1) and the NAO index (channel 2). (a) The M-SSA spectrum of the SOI and NAO index for August, along with the Monte Carlo significance test for the oscillatory modes. (b) The reconstruction of the 7.2-year mode of the M-SSA; SOI (solid), NAO index (dashed).

FIG. 10: Synchronization study of the SOI (channel 1) and the Nile River flood record (channel 2). (a) The M-SSA spectrum of the summer SOI and the Nile River record, along with the Monte Carlo significance test for the oscillatory modes. (b) The reconstruction of the 7.5-year mode of the M-SSA; SOI (solid), Nile River record (dashed). (c) Same as panel (b), for the 3.7-year mode.

FIG. 11: Sea surface temperature (SST) field in the western North Atlantic, (32^0N–43.5^0N, 75^0W–50^0W), for the 50 years between January 1958 and December 2007. The mean SST (central panel) has contour interval of 1.7 C. Composites of the 8.5-year mode, in eight phase categories are displayed clockwise around this central panel. These composites are based on the M-SSA pair (4,5), which captures 5% of the total variance (positive contours solid, negative ones dashed); the contour interval here is 0.1 C.

FIG. 12: Same as Fig. 12, but for sea surface height (SSH) in the western North Atlantic. Contour intervals are 0.1 m for the mean SSH (central panel) and 0.01 m for the composites of the 8.5-year mode in eight phase categories.

FIG. 13: The reconstructed 8.5-year oscillatory mode as a function of time, at the point ($73\ ^0$W, $37.5\ ^0$N), where its amplitude is maximal; raw data shown as the black solid line, and $RC^{(4,5)}$, which captures the oscillation, as the red solid line.

Table 1: The degree of synchronization between the first components $x_1(t)$ and $x_2(t)$ of the two coupled Rössler oscillators in Eq. (5); see text for details. The columns in the table give the variance of the first reconstructed-component (RC) pair (1,2) and of the second pair (3,4); the energy ratio $\varepsilon_{12} = E(\mathrm{RC}x_1)/E(\mathrm{RC}x_2)$ between the two components of the first RC pair; the standard deviation σ of the phase differences $d(t) = \phi_1(t) - \phi_2(t)$, and the correlation of the amplitudes A_1 and A_2 of x_1 and x_2.

Coupling parameter	Variance (%) in pair		$E(\mathrm{RC}x_1)/E(\mathrm{RC}x_2)$ in pair	σ	Amplitude correlation
C	(1,2)	(3,4)	(1,2)		
0.000	51	35	0.0	46.80	– 0.07
0.001	48	41	0.02	40.02	0.01
0.005	50	41	0.6	36.68	0.02
0.01	54	38	0.76	35.07	– 0.03
0.017	62	31	1.14	30.08	– 0.11
0.025	73	21	1.11	18.21	– 0.01
0.027	86	9	1.11	7.92	– 0.08
0.035	93	1.2	1.07	0.20	0.24
0.04	93	1.2	0.93	0.19	0.28
0.06	93	1.5	0.97	0.14	0.66
0.1	93	1.6	1.00	0.09	0.88
0.11	92	1.8	1.00	0.06	0.98

Table 2: Cross-spectral analysis of our climatic records, using M-SSA with two channels. Entries in the first column correspond to channel 1 and those in the first row to channel 2. In each cell there are three strings, separated by a comma: the first string gives the period in years of the oscillatory mode, the second string the synchronization type, and the third string is the energy ratio between channel 1 and channel 2. Oscillatory modes in the table are all significant at the 95% level or higher.

	NAO	Jerusalem	Nile River
Nile River	7.6y, FPA, 0.28		
Nile River	4.3y, FPA, 0.97		
Nile River	3.3y, FPA, 0.11		
SOI	7.2y, FPA, 0.83		7.5y, FPA, 1.64
SOI	3.7y, F, 5.3		3.7y, FP, 1.39
Jerusalem	7.8y, FPA, 2.8		
Jerusalem	3.8y, FP, 0.8		
Tree rings		12.5y, FA, 0.70	
Tree rings		7.8y, F, 0.41	
Tree rings		3.8y, F, 0.01	

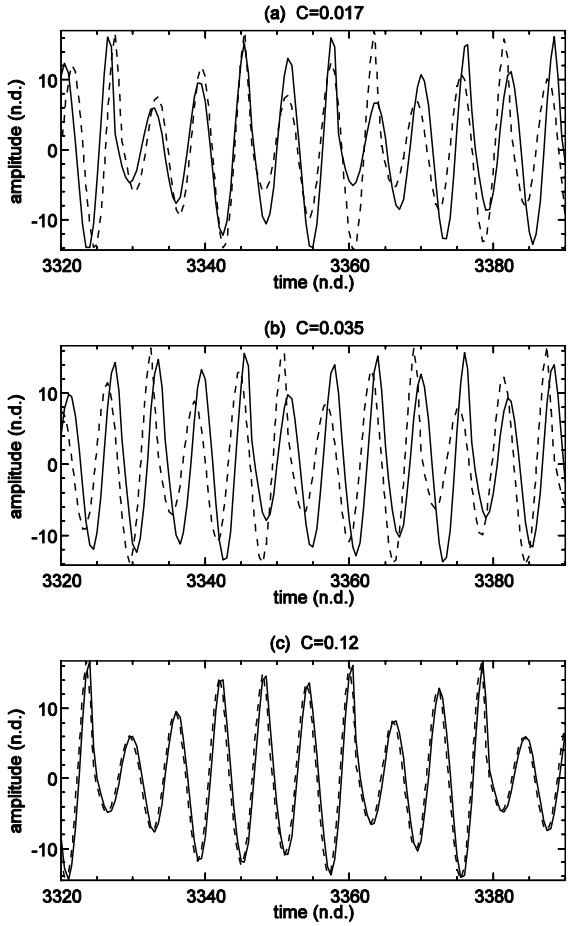
(a) C=0.017
amplitude (n.d.)
10
0
-10
3320
3340
3360
3380
time (n.d.)
(b) C=0.035
amplitude (n.d.)
10
0
-10
3320
3340
3360
3380
time (n.d.)
(c) C=0.12
amplitude (n.d.)
10
0
-10
3320
3340
3360
3380
time (n.d.)

Fig. 1

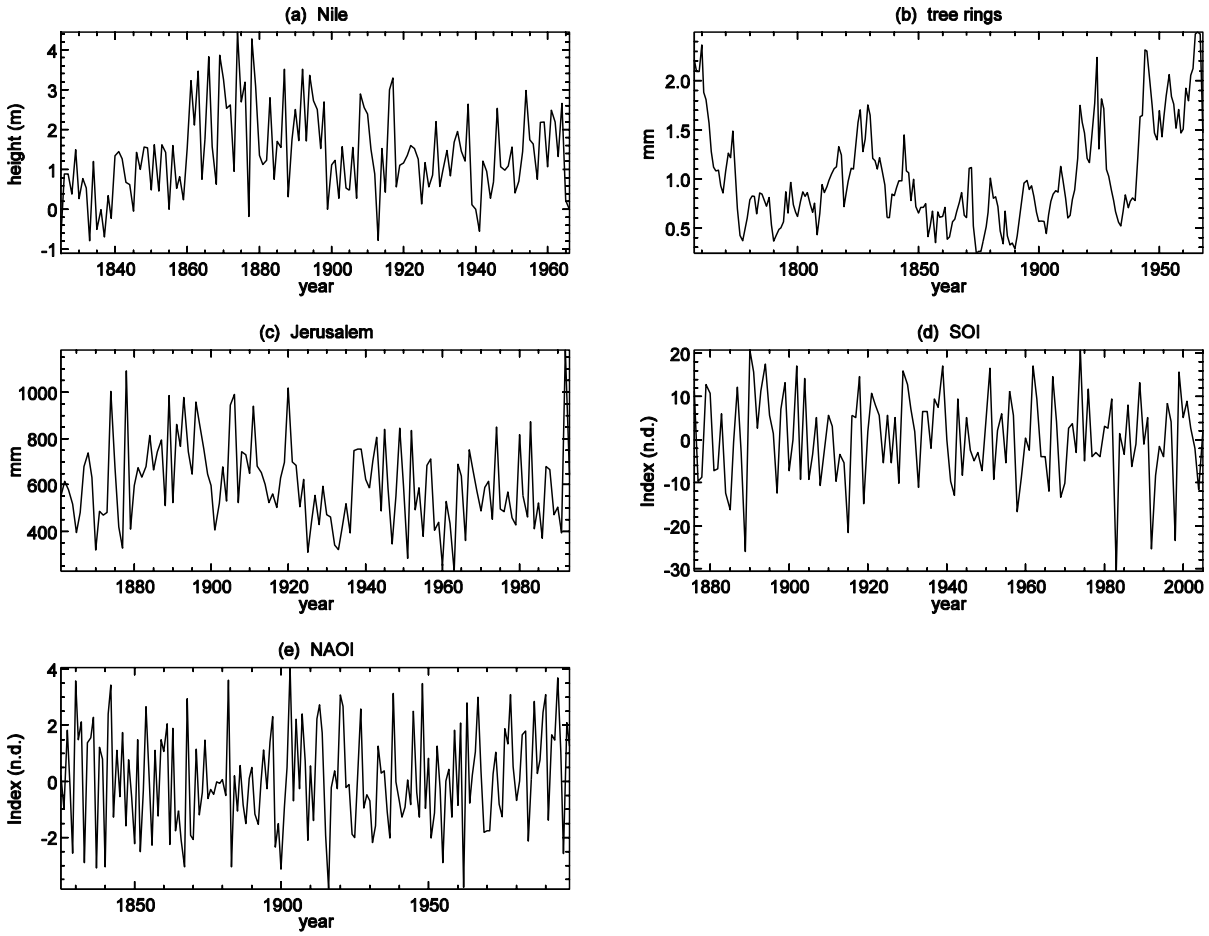
(a) Nile
height (m)
year
(b) tree rings
mm
year
(c) Jerusalem
mm
year
(d) SOI
Index (n.d.)
year
(e) NAOI
Index (n.d.)
year

Fig. 2

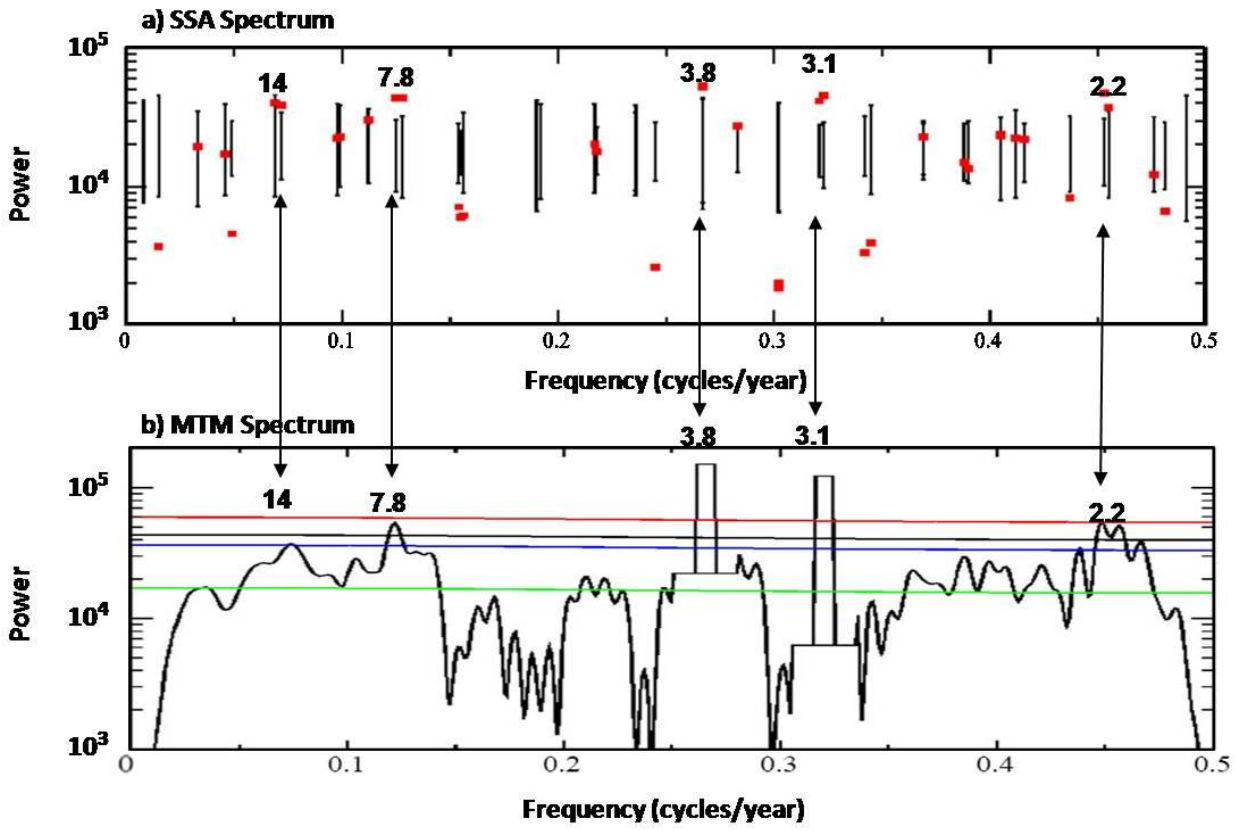
a) SSA Spectrum
Power
10^5
10^4
10^3
14
7.8
3.8
3.1
2.2
0
0.1
0.2
0.3
0.4
0.5
Frequency (cycles/year)
b) MTM Spectrum
Power
10^5
10^4
10^3
14
7.8
3.8
3.1
2.2
0
0.1
0.2
0.3
0.4
0.5
Frequency (cycles/year)

Fig. 3

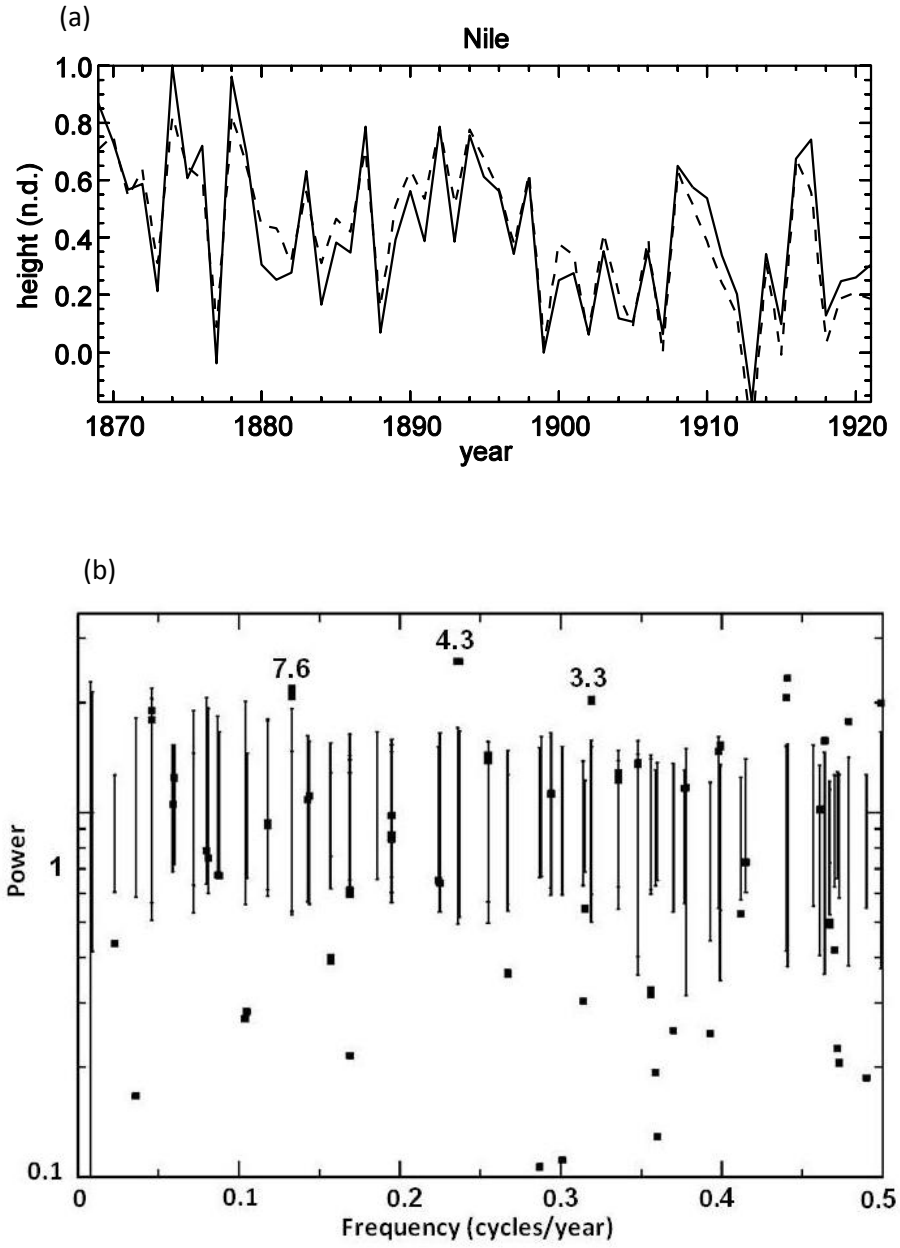
(a)
Nile
height (n.d.)
1.0
0.8
0.6
0.4
0.2
0.0
1870
1880
1890
1900
1910
1920
year
(b)
4.3
7.6
3.3
Power
1
0.1
0
0.1
0.2
0.3
0.4
0.5
Frequency (cycles/year)

Fig. 4

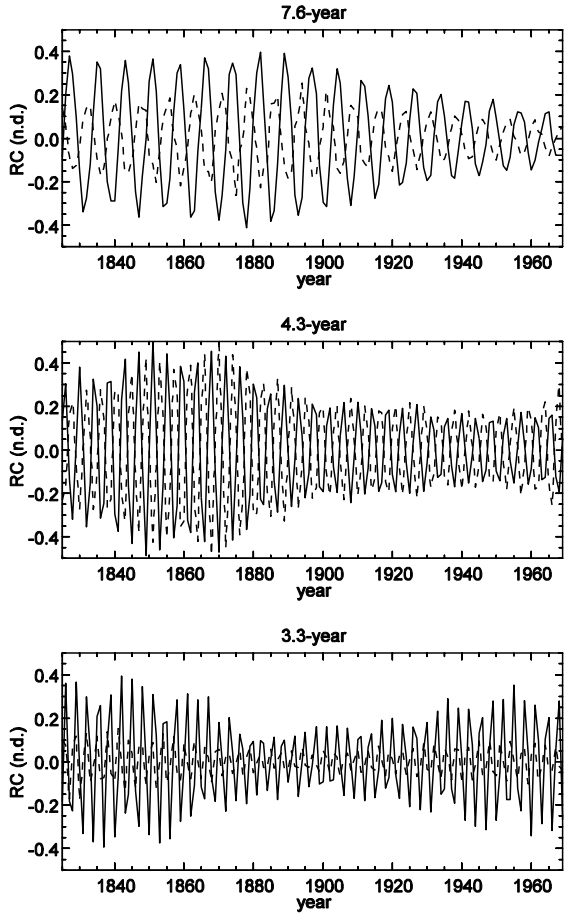
7.6-year
RC (n.d.)
0.4
0.2
0.0
-0.2
-0.4
1840
1860
1880
1900
1920
1940
1960
year
4.3-year
RC (n.d.)
0.4
0.2
0.0
-0.2
-0.4
1840
1860
1880
1900
1920
1940
1960
year
3.3-year
RC (n.d.)
0.4
0.2
0.0
-0.2
-0.4
1840
1860
1880
1900
1920
1940
1960
year

Fig. 5

(a)

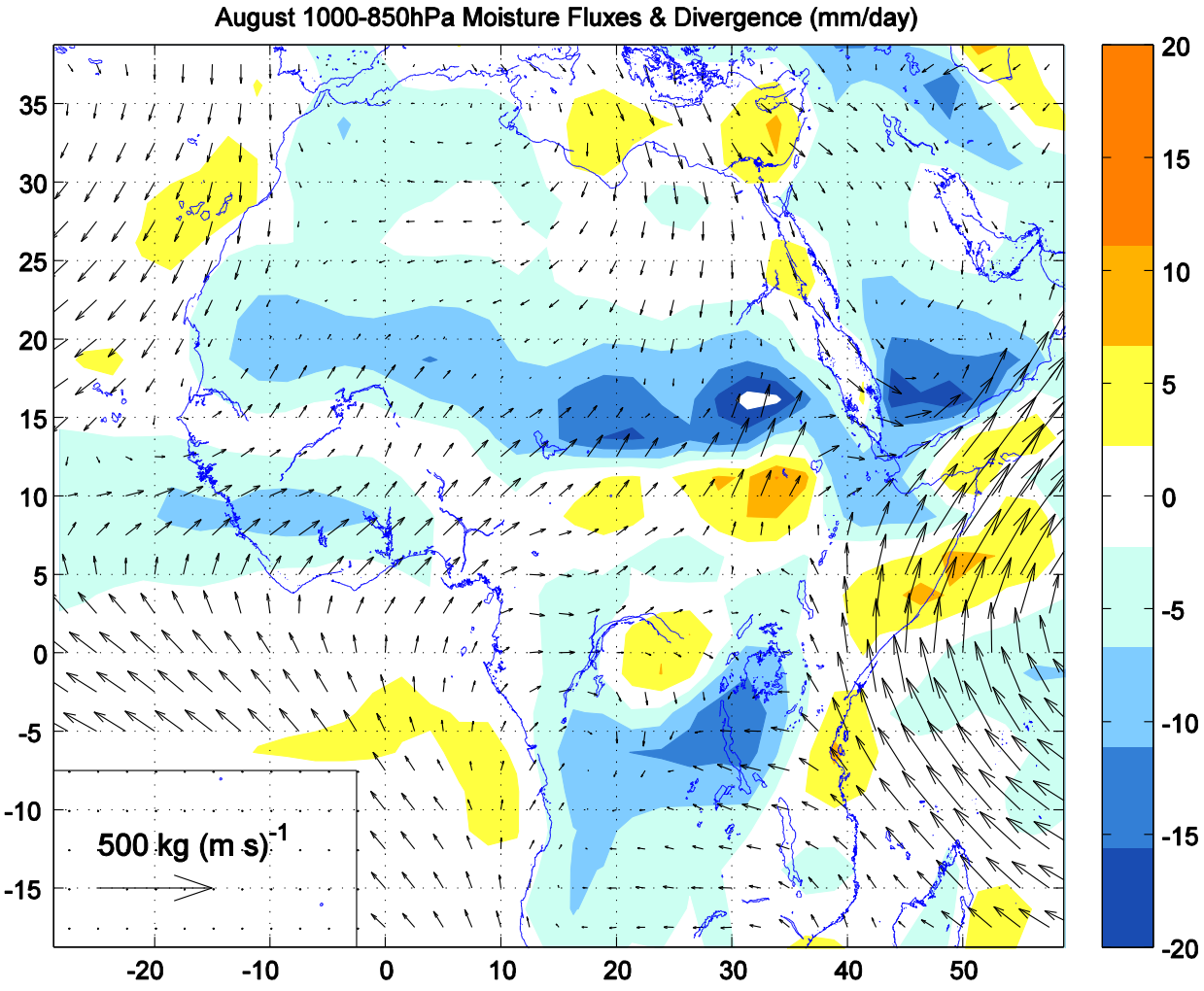
August 1000-850hPa Moisture Fluxes & Divergence (mm/day)
35
30
25
20
15
10
5
0
-5
-10
-15
-20
-10
0
10
20
30
40
50
500 kg (m s)-1
20
15
10
5
0
-5
-10
-15
-20

Fig. 6a

(b)


North Atlantic Ocean
ALGERIA
LIBYA
EGYPT
SAUDI ARABIA
IRAN
TURKEY
SUDAN
NIGER
CHAD
NIGERIA
ZAIRE
SOMALIA
YEMEN
3
2
1

Fig. 6

(a)

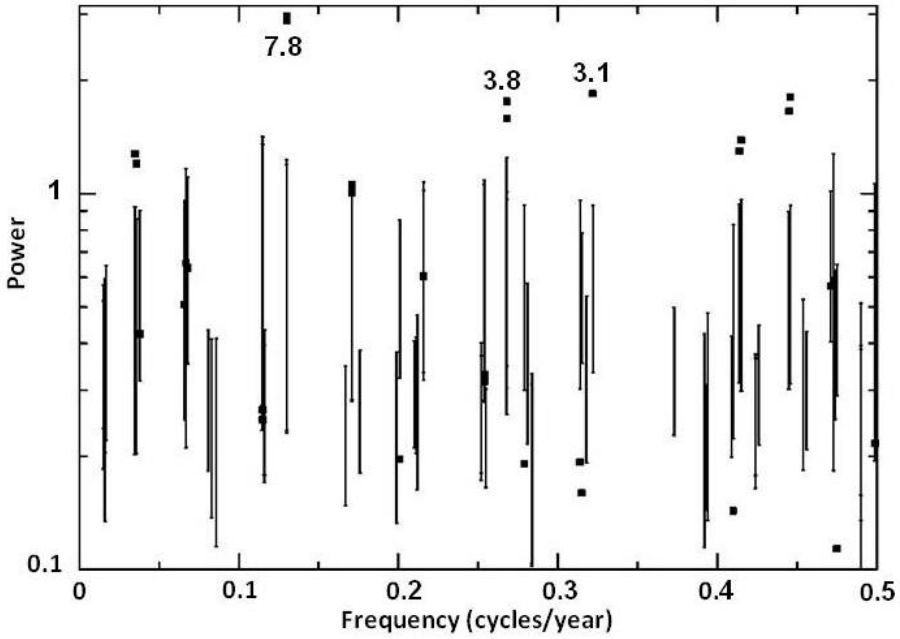
7.8
3.8
3.1
Power
1
0.1
0
0.1
0.2
0.3
0.4
0.5
Frequency (cycles/year)

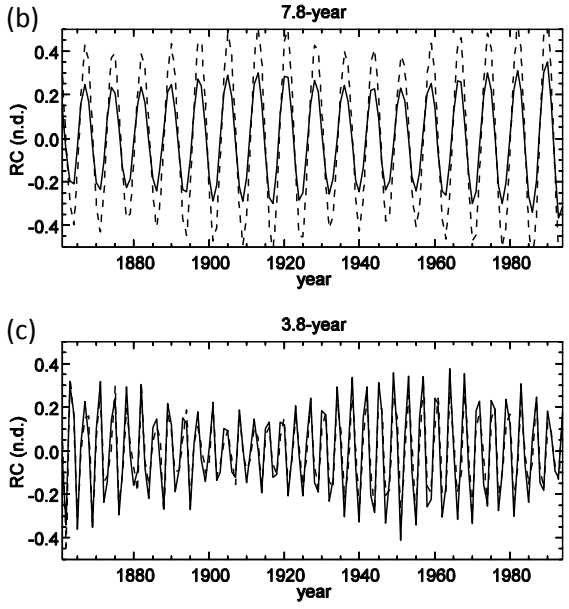
(b)
7.8-year
RC (n.d.)
0.4
0.2
0.0
-0.2
-0.4
1880
1900
1920
1940
1960
1980
year
(c)
3.8-year
RC (n.d.)
0.4
0.2
0.0
-0.2
-0.4
1880
1900
1920
1940
1960
1980
year

Fig. 7

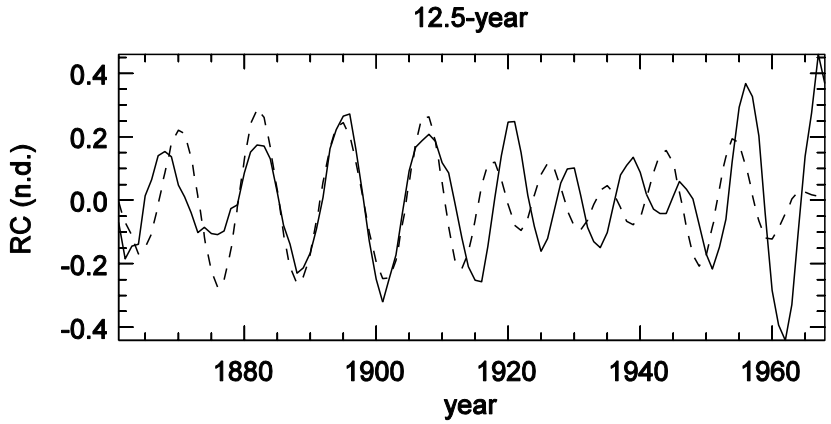

Fig. 8

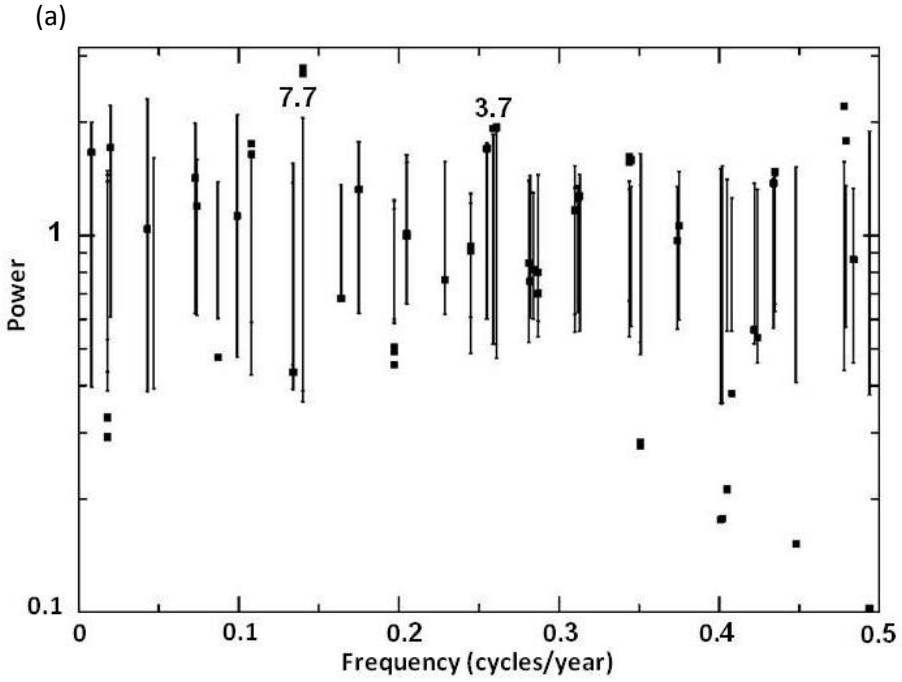
(a)
7.7
3.7
Power
1
0.1
0
0.1
0.2
0.3
0.4
0.5
Frequency (cycles/year)

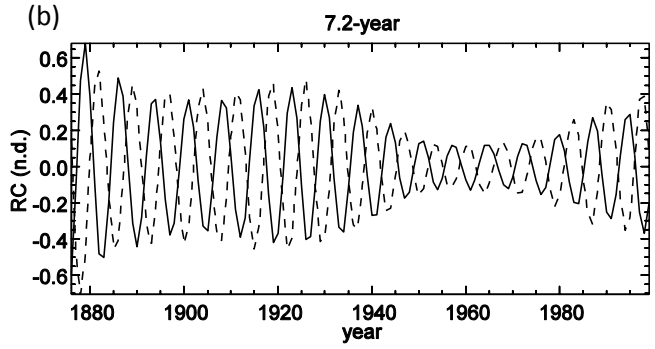
(b)
7.2-year
RC (n.d.)
0.6
0.4
0.2
0.0
-0.2
-0.4
-0.6
1880
1900
1920
1940
1960
1980
year

Fig. 9

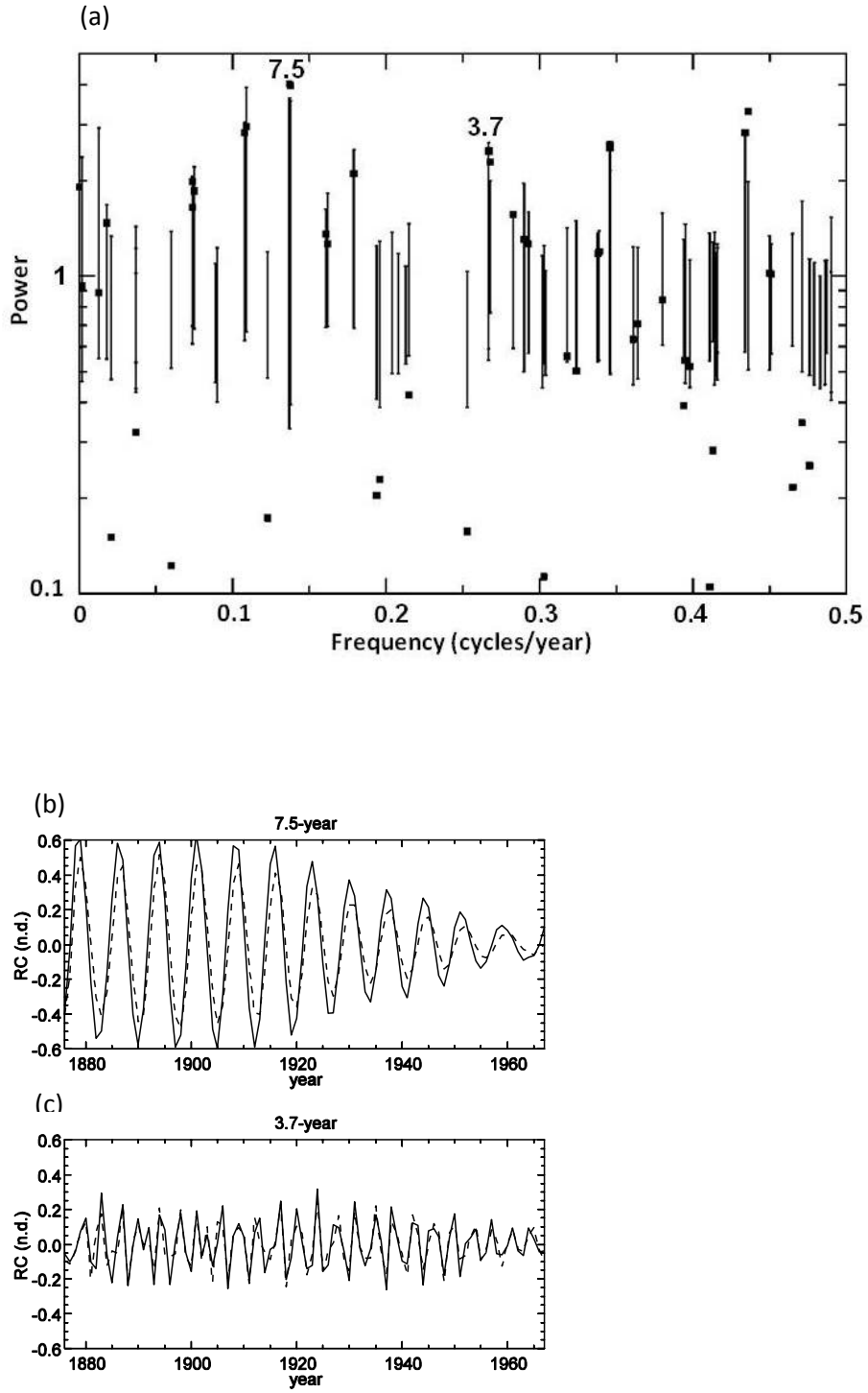
(a)
7.5
3.7
Power
1
0.1
0
0.1
0.2
0.3
0.4
0.5
Frequency (cycles/year)
(b)
7.5-year
RC (n.d.)
0.6
0.4
0.2
0.0
-0.2
-0.4
-0.6
1880
1900
1920
1940
1960
year
(c)
3.7-year
RC (n.d.)
0.6
0.4
0.2
0.0
-0.2
-0.4
-0.6
1880
1900
1920
1940
1960
year

Fig. 10

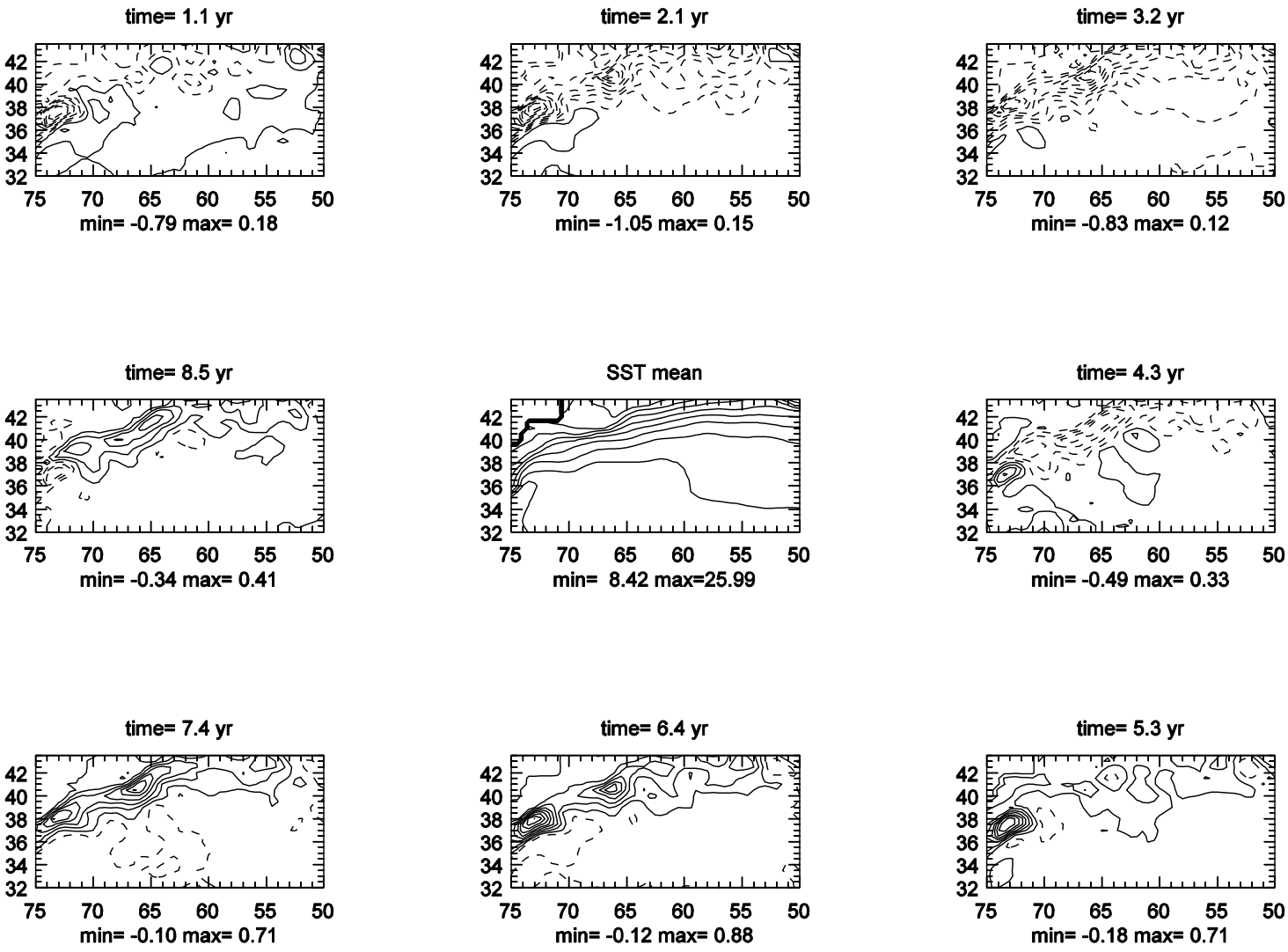
time= 1.1 yr
min= -0.79 max= 0.18
time= 2.1 yr
min= -1.05 max= 0.15
time= 3.2 yr
min= -0.83 max= 0.12
time= 8.5 yr
min= -0.34 max= 0.41
SST mean
min= 8.42 max=25.99
time= 4.3 yr
min= -0.49 max= 0.33
time= 7.4 yr
min= -0.10 max= 0.71
time= 6.4 yr
min= -0.12 max= 0.88
time= 5.3 yr
min= -0.18 max= 0.71
42
40
38
36
34
32
75
70
65
60
55
50

Fig. 11

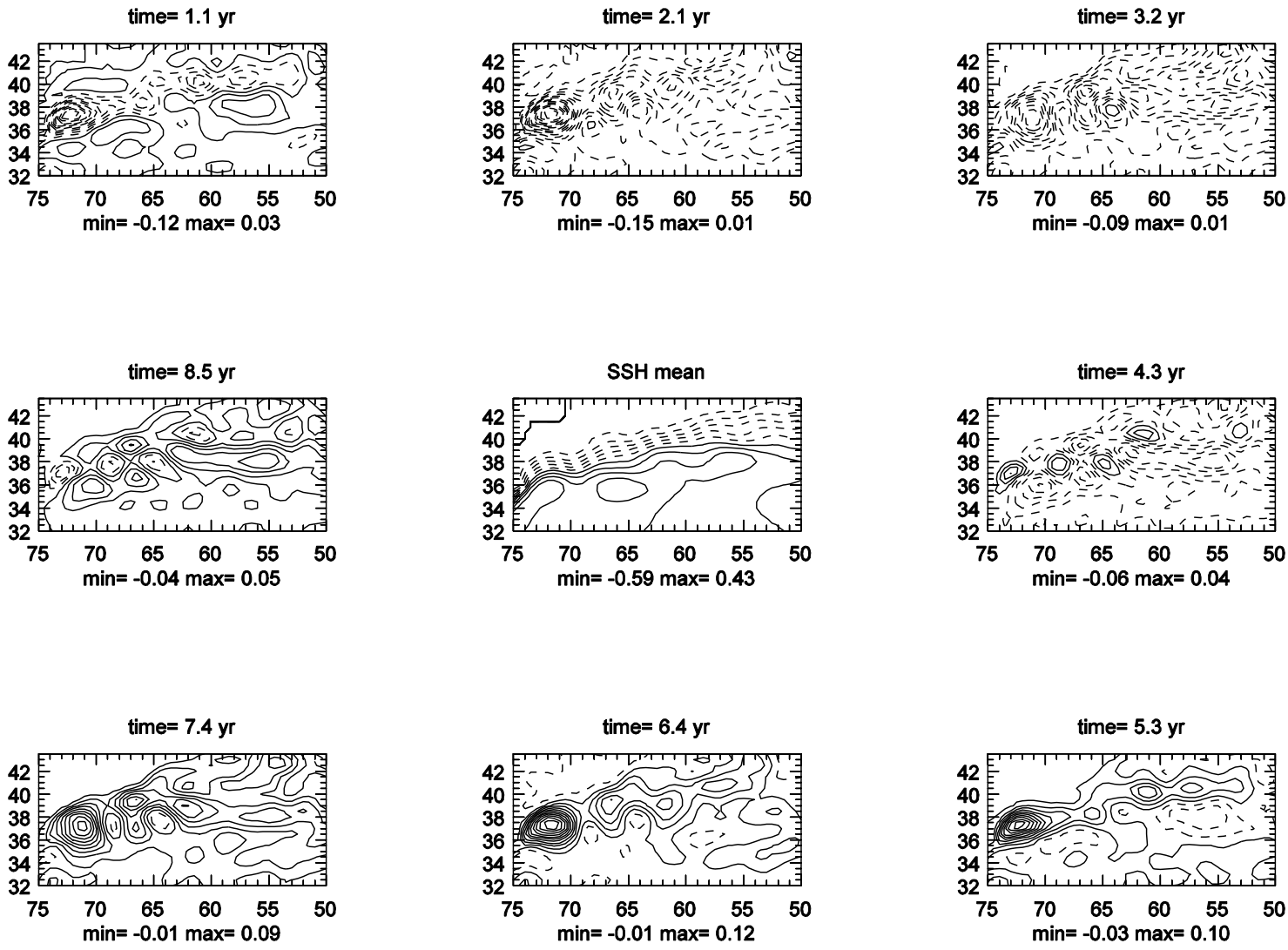
time= 1.1 yr
42
40
38
36
34
32
75 70 65 60 55 50
min= -0.12 max= 0.03
time= 2.1 yr
min= -0.15 max= 0.01
time= 3.2 yr
min= -0.09 max= 0.01
time= 8.5 yr
min= -0.04 max= 0.05
SSH mean
min= -0.59 max= 0.43
time= 4.3 yr
min= -0.06 max= 0.04
time= 7.4 yr
min= -0.01 max= 0.09
time= 6.4 yr
min= -0.01 max= 0.12
time= 5.3 yr
min= -0.03 max= 0.10

Fig. 12

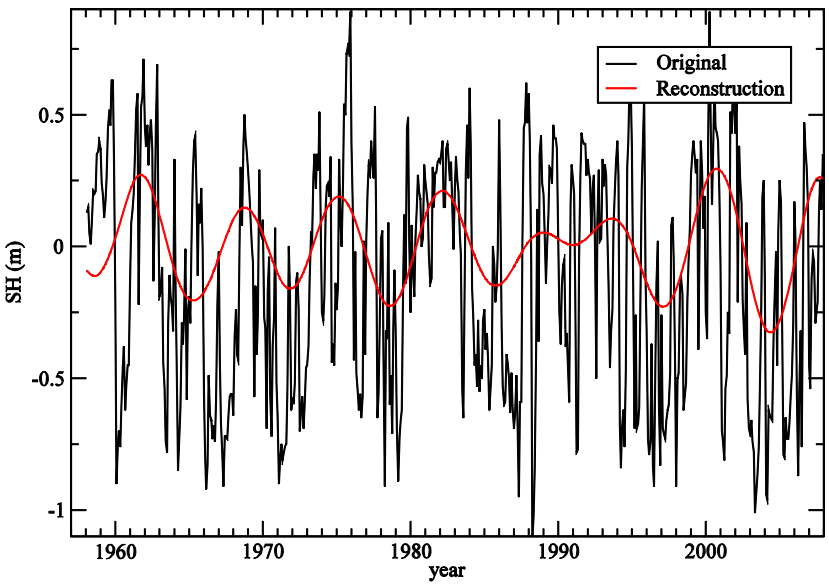
Original
Reconstruction
SH (m)
0.5
0
-0.5
-1
1960
1970
1980
1990
2000
year

Fig. 13